



# Insights from field phenotyping improve satellite remote sensing based in-season estimation of winter wheat growth and phenology

Lukas Valentin Graf<sup>a,b,\*</sup>, Quirina Noëmi Merz<sup>a</sup>, Achim Walter<sup>a</sup>, Helge Aasen<sup>a,b</sup>

<sup>a</sup> Crop Science, Institute of Agricultural Science, ETH Zurich, Universitaetstrasse 2, 8092 Zurich, Switzerland

<sup>b</sup> Earth Observation of Agroecosystems Team, Division Agroecology and Environment, Agroscope, Reckenholzstrasse 191, 8046 Zurich, Switzerland

## ARTICLE INFO

Edited by Jing M. Chen

Dataset link: [https://github.com/EOA-team/sentinel2\\_crop\\_traits](https://github.com/EOA-team/sentinel2_crop_traits)

### Keywords:

Phenotyping  
Radiative transfer modeling  
Phenology  
Leaf area index  
Canopy Chlorophyll Content  
Sentinel-2

## ABSTRACT

Timely knowledge of phenological development and crop growth is pivotal for evidence-based decision making in agriculture. We propose a near real-time approach combining radiative transfer model inversion with physiological and phenological priors from multi-year field phenotyping. Our approach allows to retrieve Green Leaf Area Index (GLAI), Canopy Chlorophyll Content (CCC) and hence Leaf Chlorophyll Content (Cab) from Sentinel-2 optical satellite imagery to quantify winter wheat growth conditions in a physiologically sound way. Phenological macro stages are based on accumulated growing degree day thresholds obtained from multi-year field phenotyping covering more than 2400 ratings from roughly 300 winter wheat varieties and reflect important physiological transitions. These include the transition from vegetative to reproductive growth and the onset of flowering, which is important information for agricultural decision support. Validation against a large data set of on-farm trials in Switzerland collected in 2019 and 2022 revealed high accuracy of our approach that produced spatio-temporally consistent results. Phenological macro stages were predicted for 970 Sentinel-2 observations reaching a weighted F1-score of 0.96. Sentinel-2 derived GLAI and CCC explained between 77 to 84% and between 79 to 84% of the variability in in-situ measurements, respectively. Here, the incorporation of phenological priors clearly increased trait retrieval accuracy. Besides, this work highlights that physiological priors, e.g., obtained by field phenotyping, can help enhancing landscape scale observations and hold potential to advance the retrieval of remotely sensed vegetation traits and in-season phenology.

## 1. Introduction

Timely knowledge of crop growth and phenological development is pivotal for evidence-based decision making in agriculture. Estimating current and historical growing conditions can increase the resource use efficiency of inputs such as fertilizer, water or pesticides (Bach and Mauser, 2018). By determining phenology and growth in a timely manner, the right amount of these inputs can be applied at the right time (Pedersen and Lind, 2017; Argento et al., 2021). Therefore, accurate, traceable and timely information about crop growth and phenology is required by many stakeholders in agriculture including agricultural agencies, insurers, individual farmers and actors from the downstream value-chain. Further, accurate estimation of crop growth plays a crucial role in global food security such as the GEOGLAM crop monitor (Becker-Reshef et al., 2020). The authors reported that the main readership included not only governments but also private sector actors such as individual farmers, demonstrating the relevance of information about crop growth at different institutional levels. Another prominent example of this is the European Union's crop monitoring

and yield forecasting JRC MARS Bulletin, which has provided crop growth information requested by stakeholders in business, academia and governmental agencies since 1993 (van der Velde et al., 2019).

Arguably, knowledge about plant growth and development is invaluable for understanding plant-environment interactions not only in agriculture but in terrestrial ecosystems in general (Zhu et al., 2016). To gain this knowledge it is essential to develop a holistic understanding of drivers of plant growth and phenology at the landscape scale. Here, it must be ensured that observed differences between geographic locations and years are caused by physiological responses of plants to their environment (Körner, 2021) and not due to differences in data quality or data processing.

In winter wheat (*Triticum aestivum*) - one of the world's most important staple crops - three major phenological stages are distinguished: germination to end of tillering (GE-ET), stem elongation to end of heading (SE-EH), and flowering to physiological maturity (FL-PM) (Hay and Kirby, 1991). The transition from tillering to stem elongation marks the transition from vegetative to reproductive growth and is important

\* Corresponding author at: Crop Science, Institute of Agricultural Science, ETH Zurich, Universitaetstrasse 2, 8092 Zurich, Switzerland.  
E-mail address: [lukasvalentin.graf@usys.ethz.ch](mailto:lukasvalentin.graf@usys.ethz.ch) (L.V. Graf).

for the timing of nitrogen fertilizer application. Moreover, the duration of SE determines the number of fertile florets (González et al., 2003), while the onset of flowering increases the susceptibility of wheat to weather-related damage such as hail (Holman et al., 2022). In addition, functional crop traits such as Green Leaf Area Index (GLAI) or Canopy Chlorophyll a+b Content (CCC) quantify growth conditions (Gitelson et al., 2014) and provide inference on secondary traits such as biomass accumulation (Gitelson et al., 2003), yield (Huang et al., 2015; Chen et al., 2018; Hashimoto et al., 2022) and nutrient supply (Delloye et al., 2018). GLAI quantifies the photosynthetically active leaf area per unit ground area and is directly proportional to gross photosynthesis (Gitelson et al., 2003). The amount of photosynthetically absorbed radiation is largely determined by CCC, which is the product of the leaf chlorophyll a+b (Cab) content of green leaves scaled-up to the canopy (Gitelson et al., 2014).

Conceptual understanding of winter wheat growth and development stems from multi-year field phenotyping experiments. Field phenotyping aims to quantitatively describe plants by a set of observable morphological, biochemical and physiological traits under natural environment conditions (Walter et al., 2015). For this purpose, imaging techniques on handheld and close-range sensing platforms are used, among others, to enable large sample sizes in trait acquisition of field crops (Araus and Cairns, 2014). It is important to note here that field phenotyping goes beyond simply collecting plant traits. In field phenotyping, plant traits are linked to environmental covariates such as air temperature or global radiation to provide a more holistic picture of plant-environment interactions. A covariate often missing in field phenotyping, however, is the continuous spatial component as experimental setups are mainly designed to understand genotype-specific (i.e., variety-specific) responses to meteorological covariates such as temperature. Differences in spatially continuous variables such as soil properties or topography and their effect on plant growth are hardly captured by current phenotyping experiments. Therefore, it remains often unclear to what degree findings from field phenotyping experiments are applicable to agricultural landscapes. Remote sensing appears as a logical tool to incorporate the missing continuous spatial component with wide-area coverage and comparably low costs of data acquisition and processing (Weiss et al., 2020). Surprisingly, research in agricultural remote sensing has so far made little use of concepts and theories from field phenotyping such as temperature-response curves (Roth et al., 2022b) and applied them on the landscape scale (Machwitz et al., 2021). For example, many remote sensing studies do not fully address underlying physiological processes that control plant growth. Arguably, bringing both fields together has huge potential (Aasen and Roth, 2022).

In the toolbox of remote sensing, physically-based radiative transfer models (RTMs) simulate plant spectral properties based on a set of leaf and canopy traits. However, the inversion of RTMs required to derive these traits from optical imagery is ill-posed, i.e., an analytical solution does not exist (Combal et al., 2002; Atzberger, 2004). To cope with ill-posedness, the usage of prior information has been highlighted to limit the range and number of potential solutions (Lauvernet et al., 2008, for example). Still, the usage of physiologically sound priors available from field phenotyping such as ratings of leaf and canopy traits has been little. A similar finding can be made for remote sensing of phenology: Phenology estimates mainly relate to mathematical properties of time series of spectral indices (de Beurs and Henebry, 2004; Garonna et al., 2016; Peng et al., 2017; Bolton et al., 2020). Remotely sensed phenology usually means Land Surface Phenology (de Beurs and Henebry, 2004) which aims to describe seasonal patterns of vegetation development by greenness proxies (Helman, 2018). Most of these remotely sensed phenology estimates therefore do not allow full physiological interpretability. As a consequence, these estimates can be difficult to compare in space and time, which is important for agricultural management. Moreover, most approaches require complete, gap-free time series (Lobert et al., 2023, for instance), which makes it

hardly possible to determine phenological phases during the growing season in near real-time (Liao et al., 2023). In-season estimates of phenology are, however, crucial for agricultural decision support due to the time-criticality of most management operations in agriculture, such as fertilizing.

To overcome the identified gaps and limitations we propose an approach combining remotely sensed imagery with multi-year field phenotyping. We focus on Sentinel-2 (S2) optical satellite imagery which has been intensively used for agricultural applications (Delloye et al., 2018; Meroni et al., 2021; Chen et al., 2022). In detail, S2 offers a high spectral resolution with 13 bands between 442 and 2202 nm. Out of these, 10 bands with a spatial resolution of 10 to 20 m can be used for analyzing vegetation parameters. Thanks to the twin constellation of the S2 A and S2B satellites, the temporal resolution reaches up to three days in mid-latitudes required to track vegetation dynamics (Frampton et al., 2013). Geographically, our research focuses on Switzerland. Switzerland is exemplary for intensively-farmed landscapes. Not only serves it as a blueprint for other highly industrialized farming systems but also for small-scale farming structures due to the small average farm (around 21 ha in 2021, (Federal Statistical Office, 2022)) and field parcel size.

Our aim is to test if concepts and theories from field phenotyping experiments can be applied at the landscape-scale using satellite remote sensing. Thus, we propose to combine the spatio-temporal component from satellite remote sensing with conceptual understanding about crop physiology and phenological macro stages from field phenotyping. This poses two specific research questions:

- First, can field phenotyping and S2 data be used to estimate phenological macro stages in-season on the landscape scale?
- Second, do physiological and phenological priors from field phenotyping improve RTM-based trait retrieval on the landscape scale?

Our paper is structured accordingly: We describe the field phenotyping, validation and remote sensing data in Section 2, which are required for setting up our workflow to combine phenotyping with satellite remote sensing. We explain the actual model calibration, inference and validation in Section 3 followed by a presentation of results in Section 4 and a discussion of these in Section 5.

## 2. Data

Based on our objective, three different types of data are required: field phenotyping data (Section 2.1), independent on-farm trial data at the landscape scale (Section 2.2), and S2 remote sensing imagery (Section 2.3).

### 2.1. Field phenotyping data

Multi-year field phenotyping data were acquired at different sites and years in Switzerland and Southern Germany. Table 1 summarizes the sites from which field phenotyping data was available.

#### 2.1.1. FIP site

Multi-year phenology data were acquired at the FIP field phenotyping site (Kirchgessner et al., 2017) located at the agricultural research station of ETH at Lindau-Eschikon (see Table 1 and red star in Fig. 1). At the FIP site Swiss and European winter wheat varieties from the GABI wheat panel (Gogna et al., 2022) are grown in two lots (lot size 36 × 40 m), allowing a randomized plot design with two full replications. Each lot is subdivided into 398 plots of 1.0 × 1.4 m, in each of which a different winter wheat variety is grown. The site is managed according to Swiss regulations for conventional farming. The site is equipped with a weather station from which temperature readings were taken.

For the beginning of SE (BBCH 31) data were available from 2020 until 2022 resulting in a total of 357 ratings. For EH (BBCH 59) data from six years (2015–2020) could be used.

**Table 1**

Overview of field phenotyping data used including site name, recorded traits, years, and number of data points (N). Abbreviations: GLAI: Green Leaf Area Index, CCC: Canopy Chlorophyll Content.

Site	Traits	Years	N	Lat [°]	Lon [°]	Reference
FIP	Phenology	2015–2022	2190	47.449	8.682	Kirchgesner et al. (2017)
SEON	GLAI, CCC, Phenology	2014	67	47.429	8.518	Liebisch et al. (2014)
MNI	GLAI, CCC, Phenology	2017–2022	70	48.267	11.7	Danner et al. (2017); Danner et al. (2019); Woche et al. (2018)
Bramenwies	GLAI, Phenology	2022	909	47.444	8.685	Wildhaber et al. (2023)

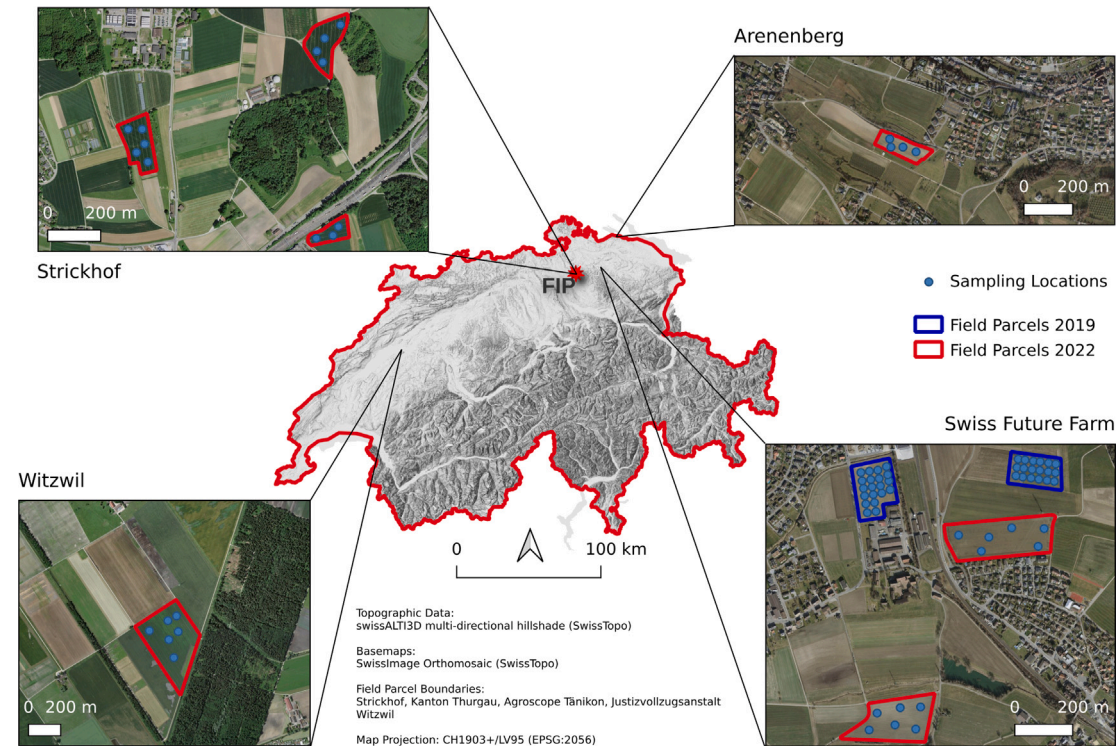


**Fig. 1.** Map of study sites of on-farm trials where in-situ samples for validation were taken in 2019 (dark blue field parcel boundaries) and 2022 (in red). The location of the FIP phenotyping site (Section 2.1.1) is denoted by a red star. (For interpretation of the references to color in this figure legend, the reader is referred to the web version of this article.)

### 2.1.2. SEON

Within the Swiss Earth Observatory Network (SEON) (Liebisch et al., 2014) GLAI, CCC and phenology was collected in 2014 at different winter wheat field parcels in north-eastern Switzerland (see Table 1) at a distance of 20 km to the FIP site (see Section 2.1.1). The data was sampled on farmers' fields managed according to Swiss agricultural practice. Weather data was available from the Swiss Meteorological Office (MeteoSwiss).

### 2.1.3. MNI

The Munich-North-Isar (MNI, Danner et al., 2019; Woche et al., 2018) dataset contains joined ratings of phenology, GLAI, and CCC from winter wheat parcels located north of the city of Munich, Germany, from five consecutive years (see Table 1). The winter wheat parcels were managed according to local agricultural practice. Meteorological data was available from a nearby weather station operated by the German National Meteorological Service (Deutscher Wetterdienst, DWD).

### 2.1.4. Bramenwies

A single winter wheat parcel managed according to Swiss conventional standards was monitored in 2022 with high spatial and temporal

sampling frequency resulting in 909 readings of phenology and GLAI (see Table 1). The parcel is located in close proximity (2 km) to the FIP site. Weather data were available from a nearby weather station.

## 2.2. On-farm trials

In-situ reference data for validating the S2-derived functional crop traits and phenological macro stages was collected in 2019 and 2022 in winter wheat field parcels distributed across Switzerland (Fig. 1). All sites are located in the Swiss midlands characterized by a temperate climate (annual mean air temperature around 10 °C) and humid conditions (annual precipitation sum around 1000 mm). Winter wheat is the most important staple crop in Switzerland. In Switzerland wheat is usually sown in October or November and harvested in July the year after.

Site characteristics are denoted in Table 2 including parcel size, winter wheat variety, management scheme, and number of sampling points. In 2022, a total of seven winter wheat parcels at four study sites was investigated and regularly monitored during the main growing season (March till June). In 2019, measurements from two winter wheat parcels located at “Swiss Future Farm” were taken (Fig. 1 lower

**Table 2**

Overview about farms and winter wheat field parcels where in-situ samples were taken for validating the S2-derived crop traits. Management codes: Conv=conventional; Org=organic; N-exp=nitrogen fertilizer experiment.

Location	Parcel	Year	Size [ha]	Variety	Management	# Sampling Points
Strickhof	Bramenwies	2022	2.04	Montalbano	Conv	4
	Hohrueti	2022	2.01	Montalbano	Conv	5
	Fluegenrain	2022	0.95	Cadlimo	Conv	3
SwissFutureFarm	Altkloster	2022	4.60	Montalbano	Conv	6
	Ruetteli	2022	3.49	Montalbano	Conv	6
	Schuerpunt	2019	2.45	Arnold	N-exp	28
	Grund	2019	1.97	Arnold	N-exp	24
Arenenberg	Broatefaeld	2022	1.48	Wiwa	Org	4
Witzwil	Parzelle 35	2022	11.98	Baretta	Conv	6

right) on April 15, 2019. These parcels were part of a nitrogen fertilization experiment and sub-divided into non-randomized treatment blocks where the effect of uniform and variable rate nitrogen fertilization on field heterogeneity was studied. The width of the treatment plots was 15 or 30 m corresponding to one or two times the operational range of the fertilizer spreader, respectively. The length varied between 40 and 90 m. The treatment zones with a width of 15 m - all of them were located at the field boundaries - were excluded from analysis. Further details about the experiment description can be found in Argento et al. (2022) and a map of the design in Figure A.9.

Meteorological data was acquired from weather stations located in close proximity to the field parcels operated by the Swiss Federal Office of Meteorology and Climatology, MeteoSwiss (Arenenberg, Swiss Future Farm, and Witzwil), and by the AgroMeteo network of the Federal Swiss Center for Excellence in Agricultural Research, Agroscope (Strickhof).

### 2.3. S2 remote sensing imagery

S2 surface reflectance data (processing level 2 A) with a scene-wide cloud cover of  $\leq 50\%$  were acquired from the Data and Information Access Services (DIAS) platform CREODIAS<sup>1</sup> between 1st of March and 31st of July 2022 and April to May 2019. All S2 scenes were atmospherically-corrected using Sen2Cor version 2.10 (payload data ground segment baseline N0400).

## 3. Methods

We start with describing how the S2 imagery (Section 3.1) was pre-processed, phenology (Section 3.2.1) and functional trait data (Section 3.2.2) were measured in-situ, and how the meteorological data were converted to thermal time (Section 3.2.3). Next, we describe the workflow from (i) model calibration using field phenotyping data (Section 3.3) to (ii) model inference on S2 imagery (Section 3.4) to (iii) model validation using data from on-farm trials (Section 3.5). The source code to reproduce the entire workflow is openly available under GNU General Public License v3.0 (see Code and Data Availability).

### 3.1. Processing of S2 imagery

We resampled the 20 m S2 bands to 10 m spatial resolution. All 10 and 20 m bands were used except band 8 (832 nm central wavelength) resulting in a total of 9 bands considered. Band 8 was disregarded in favor of band 8 A which has a higher spectral resolution and showed more accurate results in prior testing. In a next step, we clipped the S2 scenes to the extent of the field parcels using the open-source Python Earth Observation Data Analysis Library (EOdal, Graf et al., 2022). We used the scene classification layer (SCL) of the Sen2Cor output to filter out all pixels except those classified as vegetated (SCL class 4) or bare soil (SCL class 5) to avoid contamination by clouds, shadows and snow.

### 3.2. In-situ data processing

#### 3.2.1. Recording of phenology

All measurements of GLAI and CCC at the field phenotyping (Section 2.1) and on-farm trial sites (Section 2.2) were linked to phenological stages. Phenological stages were expressed using the Biologische Bundesanstalt, Bundessortenamt and CHemical Industry (BBCH) scale. At all sites the rating of BBCH stages followed the work by Lancashire et al. (1991). Here, the rating of the transition between the three phenological macro stages considered deserves further detail, i.e., the beginning of SE (BBCH stage 31) and EH (BBCH stage 59).

SE (BBCH 31) was determined by cutting the main tiller lengthwise and measuring the distance between the first node and the tillering node following the manual by Pask et al. (2012). If the distance was  $\geq 1$  cm, the stage was recorded as BBCH 31. EH (BBCH 59) was determined as the stage when the inflorescence was fully emerged. The beginning of flowering (BBCH 61) was recorded when the first anthers became visible.

#### 3.2.2. Measurement of functional traits

**Green Leaf Area Index.** GLAI was measured using destructive sampling at early growth stages and non-destructively after the onset of stem elongation (BBCH  $>33$ ). For destructive sampling, the total surface biomass of a previously defined ground surface was sampled, with plants from at least two seed rows. From five to six randomly selected wheat plants in this sample, we took the top complete developed leaf (including leaf base) and placed them on a screen with known reference area. We determined the leaf area of these leaves  $A_{leaf}$  by image segmentation, i.e., separated the leaves from the screen background. Subsequently, the total biomass as well as the leaves used for segmentation were freeze-dried for at least 48 h and their dry weight was determined ( $m_{total}$  and  $m_{leaf}$ , respectively). Using  $m_{total}$  and  $m_{leaf}$ , we computed the total leaf area and, using the known ground area  $A_{ground}$ , the GLAI (Eq. (1)).

$$GLAI = \frac{A_{leaf} * \frac{m_{total}}{m_{leaf}}}{A_{ground}} \quad (1)$$

From BBCH stage 33 onwards, this approach was no longer feasible as the increasing length of the leaves exceeded the reference grid. We therefore used a LAI-2200C Plant Canopy Analyzer by LI-COR Biosciences with a 45 degree viewing cap, performing replicates in three different orientations, each offset by 90 degrees. To avoid contamination of the measurement by direct sunlight, the measurements were mostly performed in the morning hours or under diffuse (cloudy) light conditions. A comparison of destructive and non-destructive methods was performed for individual data points and showed good agreement. GLAI measurements were continued until the onset of senescence in the lower leaf layers. Only at the SEON (Section 2.1.2) and MNI (Section 2.1.3) sites GLAI rating were continued after the onset of senescence estimating the fraction of non-photosynthetic leaf area by eye.

<sup>1</sup> <https://creodias.eu>

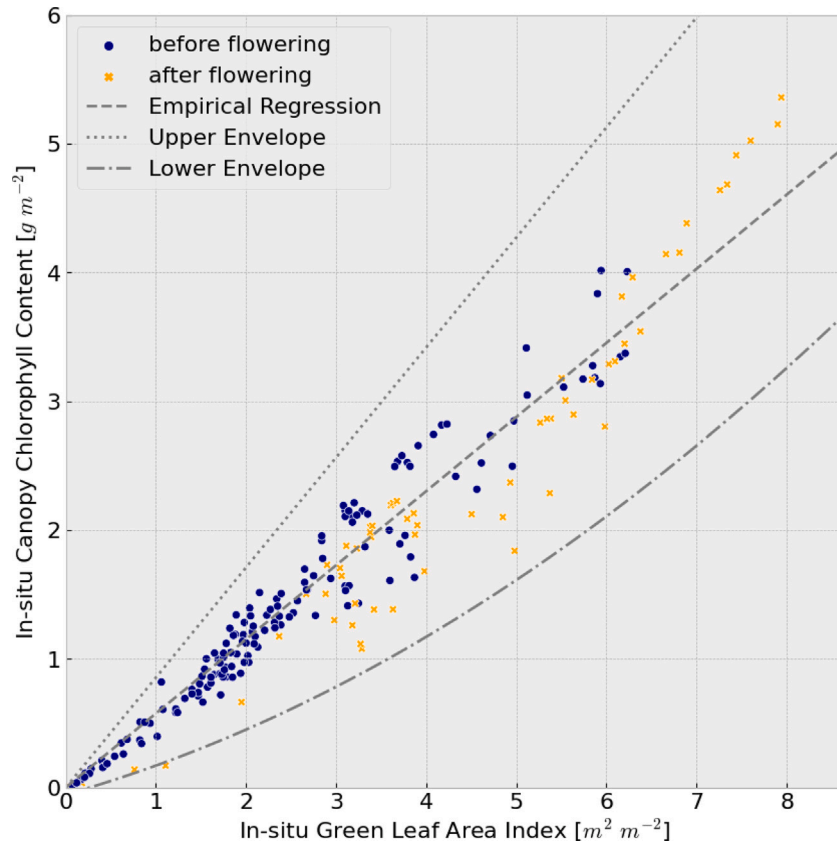


Fig. 2. Empirical relationship between CCC and GLAI (N=137) obtained from field phenotyping data. The upper and lower envelope of the data are plotted fit for the data points recorded before and after flowering, respectively.

**Canopy chlorophyll content.** CCC was estimated by destructively determining leaf chlorophyll content and GLAI. In 2019, the biomass samples were collected at experimental plots of the nitrogen fertilization experiments by Argento et al. (2022) (see Section 2.2). For each plot, leaves were randomly selected. In 2022, the entire above ground biomass of two up to four seed rows at the sampling points was collected at a pre-defined distance. A randomly selected sub-sample was used for chlorophyll analysis. In both years, immediately after sampling, the leaves were frozen. In addition, the area of these leaves was determined in the same way as for GLAI to determine leaf mass per unit area. To avoid light damage, samples were stored in the dark. The frozen samples were weighed in a cooled container and freeze dried. After freeze drying, the samples were milled and prepared for the extraction. For this process, 50 mg of the milled sample were mixed with ethanol (95%, Analytical Grade) and the supernatant was removed from the sample for the analysis. This step was repeated two times or until the remaining pellet was of white-yellowish color. In order to determine the pigment concentration in the supernatant, the absorbance of the supernatant was measured at 470 nm ( $A_{470}$ ), 649 nm ( $A_{649}$ ) and 664 nm ( $A_{664}$ ) with a Microtitre plate reader (Infinite<sup>®</sup> M1000, Tecan) using a sample volume of 200  $\mu$ l with two replicates. From the absorbance the chlorophyll a ( $c_a$ ) and b ( $c_b$ ) and a+b ( $c_{ab}$ ) content in  $\mu$ g ml<sup>-1</sup> was calculated using the formula provided by Lichtenthaler and Buschmann (2001):

$$c_a = 13.36A_{664} - 5.19A_{649} \quad (2)$$

$$c_b = 27.43A_{649} - 8.12A_{664} \quad (3)$$

$$c_{ab} = \frac{1000A_{470} - 2.13c_a - 97.64c_b}{209} \quad (4)$$

The chlorophyll concentration obtained from Eq. (4) was related to leaf area using the known probe volume (200  $\mu$ l ethanol) and weight

of the sample biomass (50 mg) dissolved in it. Using the LMA of the leaves the sample biomass was taken from we could then calculate the leaf chlorophyll content per area in  $\mu$ g cm<sup>-2</sup> and scale it up to CCC using Eq. (9). The required GLAI values were obtained from Eq. (1) based on the larger biomass samples or LI-COR measurements that were acquired in parallel to the leaf samples.

### 3.2.3. Meteorological data processing

We used the daily mean air temperature 2 m above ground ( $T_{abs,d}$ ) from weather stations to calculate growing degree days (GDD, McMaster, 1997) for winter wheat assuming a base temperature ( $T_{base}$ ) of zero degrees Celsius (Eq. (5)). We obtained accumulative GDD (AGDD) by accumulating all GDDs obtained from Eq. (5) between the sowing and harvest date as reported by field calendars at the phenotyping (Table 1) and on-farm sites (Fig. 1).

$$GDD = \begin{cases} T_{abs,d} & \text{if } T_{abs,d} > T_{base} \\ 0 & T_{abs,d} \leq T_{base} \end{cases} \quad (5)$$

### 3.3. Model calibration

For establishing physiologically plausible RTM inputs at the leaf and canopy level we consider correlations between leaf and canopy parameters (Section 3.3.1) and the dependency of GLAI to phenology and the dependency of phenology on air temperature (Section 3.3.2). All these insights are obtained from field phenotyping described in Section 2.1 using the pre-processing methods explained in Section 3.2.

#### 3.3.1. Physiological priors

CCC and GLAI are closely correlated (Gitelson et al., 2005, 2014, 2022). Following the approach proposed by Wocher et al. (2020) to

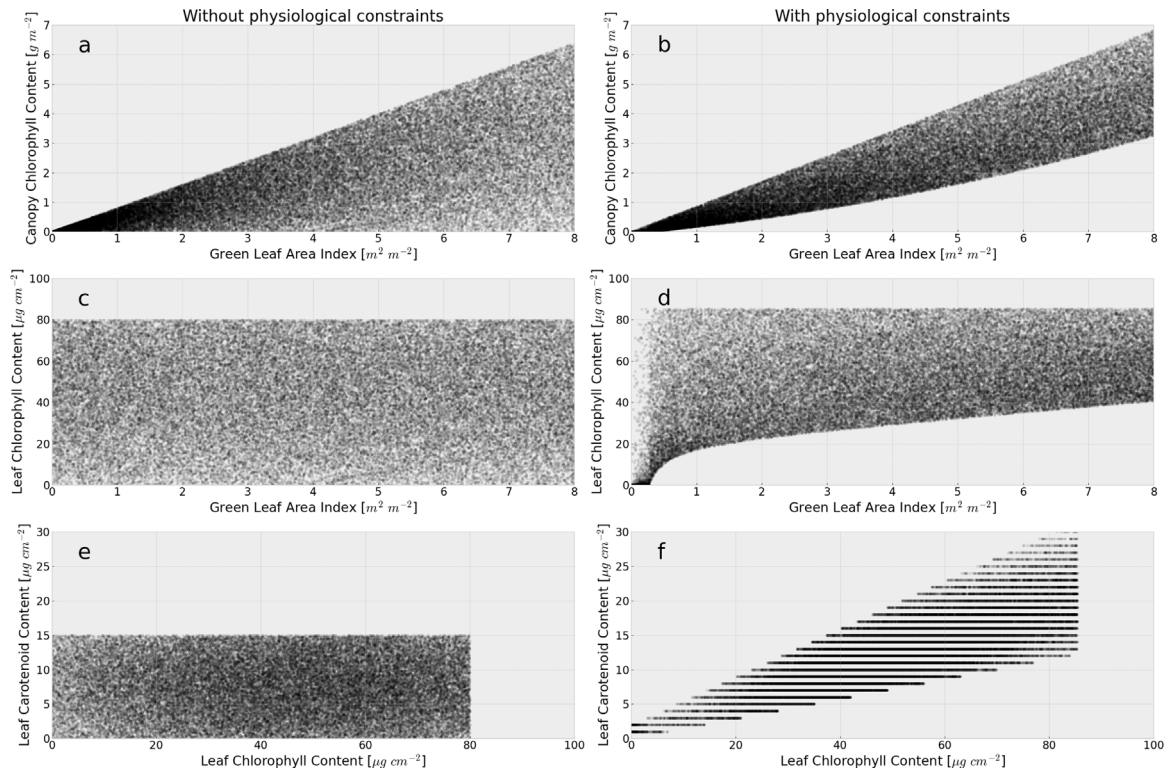


**Fig. 3.** Implementation of physiological constraints in the LUT (N=50,000) generated without phenological priors. (a) denotes the CCC-GLAI relationship without physiological constraints and (b) when the empirical relationship from Fig. 2 is enforced to redistribute CCC values. (c) shows the unrestricted relationship between Cab and GLAI and (d) the relationship when using the CCC values from (b). (e) and (f) show the redistribution of Car based on Cab (from (d)) as suggested by Wocher et al. (2020).

account for the correlation between carotenoid (Car) and Cab content we established a relationship between CCC and GLAI to increase the physiological plausibility of RTM inputs using phenotyping data from the SEON and MNI sites (see Table 1 and Sections 2.1.2 and 2.1.3).

Fig. 2 shows a strong linear relationship between CCC and GLAI obtained from field phenotyping with Pearson's  $R^2$  0.94 (N=137). We fitted a linear regression line to the data points and constructed an upper and lower envelope encompassing all data points. The linear regression with obtained coefficients is given in Eq. (6).

$$CCC = 0.5755GLAI \quad (6)$$

To fit the upper envelope, we used all CCC-GLAI pairs recorded before flowering (BBCH 61). Thus, we accounted for plant development during the vegetative (till BBCH 29) and reproductive phase in which CCC and GLAI are increasing steadily. A linear model was constructed and is denoted in Eq. (7).

$$CCC_{upper} = 0.8544GLAI \quad (7)$$

For the lower envelope we used all CCC-GLAI pairs recorded after BBCH 61. Here, we assume CCC and GLAI to decline with onset of senescence. We used a second order polynomial to construct the envelope (Eq. (8)). The reason for choosing a linear and polynomial model for the upper and lower envelope, respectively, follows the reasoning by Gitelson et al. (2014): During vegetative growth stages, the relationship between GLAI and CCC is strongly linear but tends to become polynomial for reproductive stages after flowering due to hysteresis effects.

$$CCC_{lower} = 0.0763 * \left( \frac{GLAI}{1.6819} \right)^2 + 0.3336 * \frac{GLAI}{1.6819} - 0.0551 \quad (8)$$

Following the approach by Wocher et al. (2020) we used the regression line and the envelopes to distribute CCC values using a truncated Laplacian distribution based on GLAI. Fig. 3 illustrates the principle: The left column in Fig. 3(a, c, e) shows the relationship between

**Table 3**

Statistics of GLAI values in  $m^2 m^{-2}$  for phenological macro stages and all stages derived from phenotyping data of winter wheat (N=909). Corresponding BBCH ranges are denoted in brackets.

Phenology	5% Quantile	Median	95% Quantile	N
GE-ET (0–29)	0.0	0.6	2.0	189
SE-EH (31–59)	0.5	4.2	6.5	661
FL-PM (61–99)	0.3	6.3	8.0	166
all (0–99)	0.0	3.8	8.0	909

CCC and GLAI (a), Cab and GLAI (c), and Car and Cab (e), when no physiological priors are included and the traits are, thus, uncorrelated. Here, a truncated normal distribution is assumed for Cab ( $\mathcal{N}(50, 40)$   $\mu g cm^{-2}$ ) with a minimum of 0 and maximum of 80  $\mu g cm^{-2}$  as suggested by Danner et al. (2021). Based on the same reference we obtained the uncorrelated Car samples (Fig. 3e) with a minimum of 0 and maximum of 15  $\mu g cm^{-2}$  using ( $\mathcal{N}(7.5, 5)$   $\mu g cm^{-2}$ ). Our proposed workflow starts at Fig. 3a with the redistribution of the CCC values based on the empirical relationship from Fig. 2 using Eqs. (6) to (8). The result is shown in Fig. 3b: Low CCC values do not occur when GLAI values are high, which is consistent with the literature (Gitelson et al., 2014). Using the redistributed CCC from Fig. 3b, we redistributed Cab, using:

$$CCC (g cm^{-2}) = Cab * GLAI * 0.01 \quad (9)$$

which can be rewritten to

$$Cab (\mu g cm^2) = \frac{CCC}{GLAI} * 100 \quad (10)$$

to calculate Cab from CCC and GLAI. The result is shown in Fig. 3d: Low Cab values are removed when GLAI is high. In a last step, we used the redistributed Cab to implement the Car-Cab relation described in Wocher et al. (2020). The result is depicted in Fig. 3f. Thus, based on GLAI, CCC, Cab and Car are redistributed and mutually correlated based on empirical relationships from field phenotyping to establish physiologically plausible RTM inputs.

**Table 4**  
AGDD statistics (in °C) for begin of SE (BBCH 31) and EH(BBCH 59) derived from field phenotyping data at the FIP site.

Phenological Stage	BBCH Code	5% Quantile	Median	95% Quantile	N
Begin of Stem Elongation	31	737	803	870	357
End of Heading	59	1382	1487	1602	1833

### 3.3.2. Phenological priors

**Dependency of GLAI on phenology.** As described in Section 2.1, CCC at the canopy as well as Cab and Car at the leaf scale are distributed based on GLAI (Fig. 3b, d, f). GLAI in turn depends on phenology. From the SEON, MNI and Bramenwies datasets (see Table 1 and Sections 2.1.2 to 2.1.4) we analyzed the measured GLAI values using the 5, 50 and 95% quantile. Analysis was carried out for all phenological stages (BBCH 0–99), as well as for GE-ET (BBCH 0–29), SE-EH (BBCH 31–59) and FL-PM (BBCH 61–99). The obtained descriptive statistics are shown in Table 3.

**Dependency of phenology on air temperature.** Air temperature is an important driver of plant growth and phenological development (Parent and Tardieu, 2012; Roth et al., 2022a). We used the FIP field phenotyping data about the beginning of SE (BBCH 31) and EH (BBCH 59) to obtain descriptive statistics of the AGDD required for a winter wheat cultivar to reach these phenological stages. The descriptive statistics showing the 5, 50 and 95% quantile are summarized in Table 4.

### 3.3.3. Radiative transfer modeling

We used the PROSAIL RTM (Jacquemoud et al., 2009) coupling the PROSPECT-D leaf RTM (Féret et al., 2017) with the 4SAIL (Verhoef, 1984) canopy RTM to simulate winter wheat directional reflectance based on the proposed physiological and phenological priors (Sections 3.3.1 and 3.3.2). PROSAIL is a one-dimensional RTM based on the turbid medium assumption meaning that canopies are treated as two-dimensional layers with scattering and absorbing particles. Three-dimensional structural effects are neglected. Viewing and illumination angles were set to scene-specific values. In PROSAIL, chlorophyll content is a leaf variable, Cab, (i.e., a variable of PROSPECT-D) given in  $\mu\text{g cm}^{-2}$ . For scaling up to the canopy, we calculated CCC (in  $\text{g m}^{-2}$ ) based on GLAI (Eq. (9)).

Table 5 shows the leaf (PROSPECT-D) and canopy (4SAIL) parameters input into PROSAIL. The range of GLAI values denoted in Table 5 is set to the range found for all phenological phases (BBCH 0–99). For the phenological macro stages, the range of GLAI values is modified according to the 5%–95% quantile range denoted in Table 3 (see Section 3.3.2) to integrate the phenological prior. In all phenological stages GLAI is distributed uniformly. Leaf parameters Cab and Car are redistributed based on GLAI as described in Section 3.3.1 to ensure physiological plausibility of PROSAIL simulations. The remaining parameters are set to values provided by Woche et al. (2020) and Danner et al. (2021), which are also based on in-situ data including winter wheat samples.

Thus, for each S2 scene we generated four lookup tables (LUTs): Three LUTs for the phenological macro stages (GE-ET, SE-EH, FL-PM) and a single LUT for all stages (BBCH 0–99). We used a fully randomized sampling scheme to generate input pairs of leaf and canopy parameters from Table 5 to run PROSAIL in forward mode. After running PROSAIL, we carried out further post-processing: We discarded simulated spectra that had a physiologically unrealistic blue shift of the green reflectance peak as proposed by Woche et al. (2020). In detail, Woche et al. (2020) analyzed data from handheld field spectrometers, airborne hyperspectral imaging sensors and the ANGERS leaf optical dataset (Jacquemoud et al., 2003). They observed that green reflectance peaks of vegetation do not occur at wavelengths  $< 547$  nm. PROSAIL, however, sometimes simulates vegetation spectra in which the green peak is shifted towards shorter wavelengths (i.e.,  $< 547$  nm). This may be an indication of physiologically implausible input parameter combinations or a modeling artifact. Due to inadmissible shifts of

**Table 5**

Parameter ranges and distributions for the combined leaf (PROSPECT-D) and canopy (4SAIL) RTM (PROSAIL) without phenological priors applied to GLAI. The ranges are given for uniform distributions (range) or a truncated Gaussian distribution with mean and standard deviation denoted in brackets. Cab and Car are redistributed on GLAI as shown in Fig. 3 and explained in Section 3.3.1.

Trait	Description	Unit	Range
PROSPECT-D (Leaf)			
N	Leaf Structure Parameter	[-]	1–2.5 (1.5, 0.2)
Cab	Leaf Chlorophyll a+b Content	$[\mu\text{g cm}^{-2}]$	redistributed based on GLAI
Car	Leaf Carotenoid Content	$[\mu\text{g cm}^{-2}]$	redistributed based on Cab
Cant	Leaf Anthocyanin Content	$[\mu\text{g cm}^{-2}]$	0.0–5.0 (2.0, 0.8)
Cbrown	Brown Pigments	[-]	0–1
Cw	Equivalent Water Thickness	[cm]	0–0.07 (0.04, 0.02)
Dm	Dry Matter Content	$[\text{g cm}^{-2}]$	0–0.01
4SAIL (Canopy)			
GLAI	Green Leaf Area Index	$[\text{m}^2 \text{m}^{-2}]$	0–8
ALA	Leaf Inclination Angle	[deg]	30–70
hspot	Hot spot Parameter	[-]	0.01–0.5
rsoil	Soil Brightness Factor	[-]	0–1
psoil	Dry/Wet Soil Factor	[-]	0–1

the green peak, we discarded around 5% of the simulated S2 spectra. This is clearly lower than the number of 23% of invalid spectra reported by Woche et al. (2020) suggesting that physiological priors reduce the amount of implausible PROSAIL spectra.

The remaining 1 nm PROSAIL outputs were resampled to the spectral response functions of S2A and S2B provided by ESA. Input parameters and simulated S2 spectra were stored in LUTs for RTM inversion.

## 3.4. Model inference

For inference on S2 imagery, three scenarios were run: The first scenario setup uses a single RTM parametrization for the entire growing season (NO-PHENO). In the second scenario we use AGDDs for estimating the onset of phenological stages and use the LUT of the macro stage (AGDD-PHENO). The third scenario is essentially the same as the second but includes spatial detail from S2 pixel-based cost function values (see Section 3.4.2) to test if differences in phenological transitions can be detected within the field parcels (AGDD-S2-PHENO).

### 3.4.1. RTM inversion

For each S2 scene we obtained GLAI, CCC and hence Cab using the simulated S2 LUTs. We took the median of the  $n$  best solutions in terms of the smallest cost function values between observed and simulated S2 spectra. As cost function we used the root mean squared error (RMSE) between S2 observed ( $p$ ) and PROSAIL simulated spectra ( $q$ ) considering all  $\lambda_1, \dots, \lambda_m$  spectral bands of S2 used ( $m = 9$ , see Section 2.3):

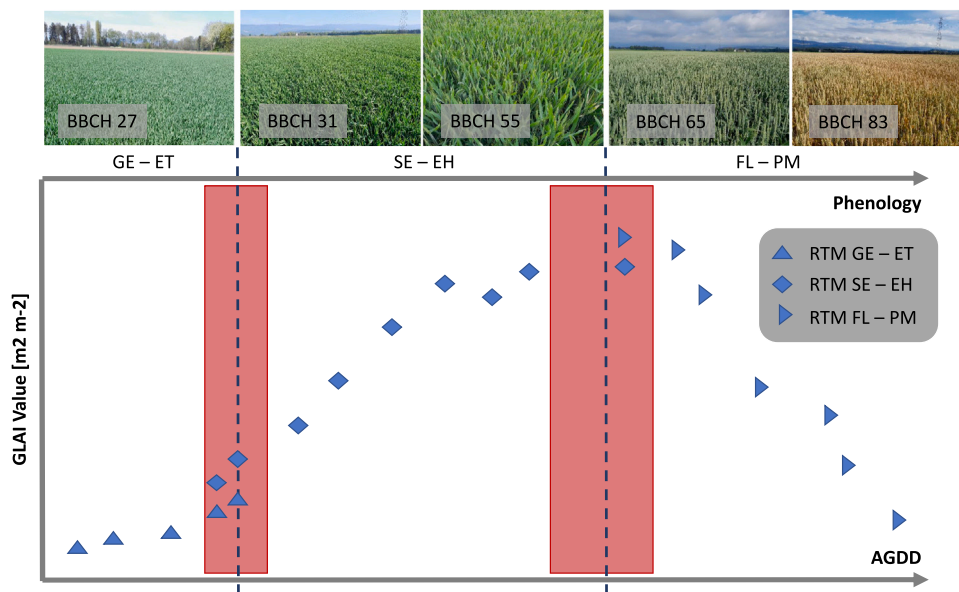
$$RMSE = \sqrt{\frac{\sum_{\lambda_i=1}^{\lambda_m} (p(\lambda_i) - q(\lambda_i))^2}{m}} \quad (11)$$

Table 6 shows the configurations used for the phenological phases (scenarios AGDD-PHENO and AGDD-S2-PHENO) and the NO-PHENO scenario. The configurations were obtained from systematic testing of different cost functions, LUT sizes and number of solutions of the inversion (see Table A.9 in Appendix A). We optimized for enhancing the correlation between modeled and in-situ observed GLAI values in terms of Pearson's R-square  $R^2$ .

**Table 6**

Setup of the LUT-based inversion for the phenological phases including the cost function, LUT size, and the scenario the LUT was used for (RMSE: root mean squared error, MAE: mean absolute error). The BBCH ranges are denoted in brackets.

Phenology	Cost Function	LUT size	No. Solutions	Scenarios
GE-ET (0–29)	RMSE	10000	100	AGDD-PHENO, AGDD-S2-PHENO
SE-EH (31–59)	MAE	50000	5000	AGDD-PHENO, AGDD-S2-PHENO
FL-PM (61–99)	MAE	50000	5000	AGDD-PHENO, AGDD-S2-PHENO
all (0–99)	MAE	50000	5000	NO-PHENO



**Fig. 4.** Proposed workflow for estimating the transition between main phenological stages in winter wheat based on accumulated growing degree days (AGDD) and GLAI trajectories from RTM inversion. The red rectangles denote AGDD windows where transitions from tillering to stem elongation and from heading to flowering most likely occur based on phenotyping experiments. The dashed lines denote the median AGDD for these transitions. Examples of winter wheat canopies at different development stages (expressed in BBCH codes) are shown in the top row in addition.

### 3.4.2. Phenology retrieval

In the NO-PHENO scenario a single RTM parametrization was used for all S2 scenes to derive GLAI and CCC. In the other two scenarios we had to determine the phenological macro stage to select the appropriate LUT for RTM inversion. Fig. 4 highlights the procedure for a hypothetical S2-derived trait time series. The red rectangles define the AGDD ranges identified from field phenotyping (Table 4) where a switch between the phenological stages most likely occurs. In the AGDD-PHENO scenario we used the median AGDD obtained from Table 4 to switch between the phenological phases (dashed lines in Fig. 4). In the AGDD-S2-PHENO scenario we used the value of cost function of the RTM inversion in addition. I.e., in the AGDD window of beginning of SE (BBCH31) we compared the median cost function value from inverting the LUT for the tillering phase (GE-ET, BBCH 0–29) with the value obtained from SE-EH (BBCH 31–59). If the latter was lower, we switched from tillering into stem elongation. Otherwise the observation remained in the tillering phase until either the cost function value from stem elongation was lower or the end of the critical AGDD was reached. In that case, a switch was forced. In case no S2 scene was available we used the same procedure as in AGDD-PHENO.

## 3.5. Model validation

### 3.5.1. On-farm trial data processing

Independent measurements of GLAI, CCC and BBCH were recorded at weekly to bi-weekly intervals at on-farm locations in Switzerland (see Fig. 1 and Table 2) using the methods described in Section 3.2. These measurements are used to test the accuracy of models calibrated on field phenotyping data applied to S2 imagery at the landscape scale (see Section 3.5.2).

### 3.5.2. Comparison of satellite and in-situ data

Modeled GLAI, CCC and phenological macro stages were compared against on-farm validation data (see Section 2.2). We used a maximum difference of 20 GDD between in-situ sampling dates and S2 overpasses which corresponds to a maximum temporal difference of one up to a couple of days depending on the time of the year. For spatial intersection, we constructed a circle with 10 m radius around the point coordinate of the in-situ measurement. We used the mean of all S2 pixels that overlapped this circle. This is to ensure that the influence of uncertainties in the positional accuracy of both data sources is minimized.

We then calculated common error metrics including the root mean squared error (RMSE), normalized RMSE (nRMSE), normalized absolute median deviation (NMAD) and  $R^2$  to compare modeled GLAI and CCC to in-situ samples. We treated the retrieval of the three phenological macro stages as a classification problem, i.e., a segmentation of the growing season into three stages, in which the true phenological macro stage obtained from the BBCH ratings served as target class label. We calculated the confusion matrix, the F1-score per phenological stage, i.e., per class, and an adjusted F1-score accounting for class imbalances to quantify model performance using phenological data from 2022. For a single class classification problem, i.e., a single phenological phase, the F1-score is the harmonic mean of precision (positive predictive value) and recall (true positive rate) calculated from the number of true and false positives (tp, fp), as well as true and false negatives (tn, fn).

$$precision = \frac{tp}{tp + fp} \quad (12)$$

$$recall = \frac{tp}{tp + fn} \quad (13)$$

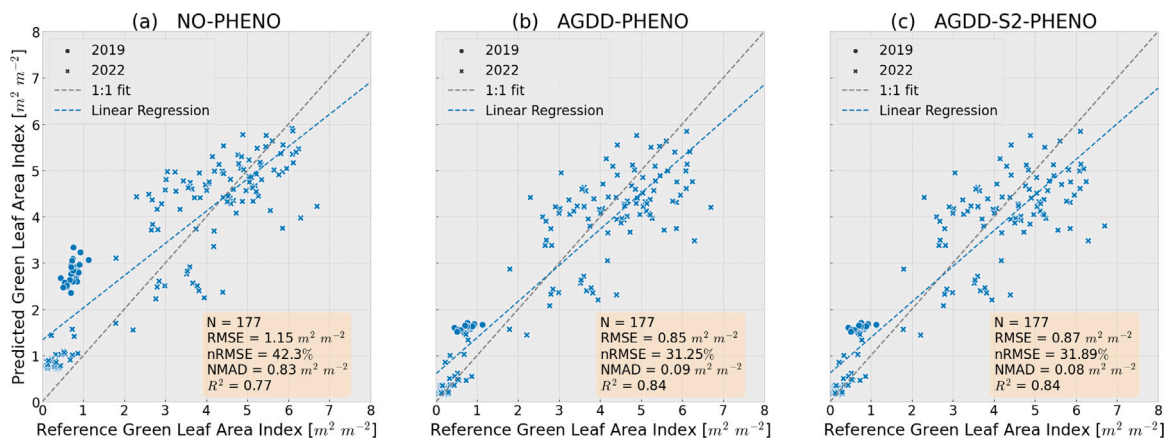


Fig. 5. Scatter plots between in-situ reference and RTM-derived GLAI for the NO-PHENO (a), AGDD-PHENO (b), and AGDD-S2-PHENO (c) scenarios. The year the data was collected is denoted by dots (2019) and crosses (2022).

Table 7

Confusion matrix showing in-situ rated and AGDD-PHENO predicted phenological macro stages for sampling dates in 2022 with S2 imagery available (N=148).

		AGDD-PHENO Predicted		
		GE - ET	SE - EH	FL - PM
In-Situ Rated	GE - ET	42	6	0
	SE - EH	0	61	0
	FL - PM	0	0	39

Table 8

Confusion matrix showing in-situ rated and AGDD-S2-PHENO predicted phenological macro stages for sampling dates in 2022 with S2 imagery available (N=148).

		AGDD-S2-PHENO Predicted		
		GE - ET	SE - EH	FL - PM
In-Situ Rated	GE - ET	42	6	0
	SE - EH	0	61	0
	FL - PM	0	3	36

$$F1_{score} = \frac{2 \times precision \times recall}{precision + recall} \quad (14)$$

For a multi-class classification problem as in this study, the adjusted F1-score is calculated from the F1-scores per class weighted by the number of samples per class. The adjusted F1-score is thus a measure for the overall performance of the phenological model. Error metrics were provided for all three experimental setups to test the effect of phenological priors on RTM inversion accuracy and determine the most accurate method for phenology estimation.

## 4. Results

### 4.1. Phenological macro stages

From a total of 970 S2 observations over the sampling points (Table 2), 134 (14%) were located in the AGDD windows determined from phenotyping (Table 4). The number is based on the requirement that a S2 observation must be within  $\pm 20$  AGDD to an in-situ observation. In the GE-ET to SE-EH transition window 23 out of 80 S2 observations could be compared to in-situ BBCH ratings. In the second window (SE-EH to FL-PM) it was 8 out of 54 observations.

The purely temperature-based AGDD-PHENO scenario predicted nearly all three stages correctly resulting in an adjusted, i.e., multi-class, F1-score of 0.96. In detail, the class-specific F1-score for GE-ET was 0.93, 0.95 for SE-EH and 1.0 for FL-PM. The confusion matrix is shown in Table 7 comparing in-situ rated macro stages to model predictions. Six out of 42 observations (14%) were wrongly assigned to the SE-EH stage by the model as can be seen in the confusion matrix (Table 7). For the second transition all data points were assigned to the correct phenological macro stage.

The performance of the AGDD-S2-PHENO scenario was slightly lower as shown in the confusion matrix in Table 8. This was due to an additional confusion in the second transition window of three observations. Still, the adjusted, i.e., multi-class, F1-score of the AGDD-S2-PHENO model was 0.94 as most observations were assigned correctly

based on AGDDs. For the single phenological stages, the F1-score was 0.93, 0.93, and 0.96, for GE-ET, SE-EH, and FL-PM, respectively.

### 4.2. Functional trait retrieval

#### 4.2.1. Green leaf area index

The accuracy of GLAI prediction increases by adding phenological priors. Fig. 5 shows scatter plots of in-situ measured GLAI on the x-axis and GLAI from PROSAIL inversion on the y-axis for the three scenario setups. In the baseline scenario without phenology (NO-PHENO), the RMSE is  $1.15 \text{ m}^2 \text{ m}^{-2}$  (nRMSE: 42.30%) and the NMAD is  $0.77 \text{ m}^2 \text{ m}^{-2}$ . The scenarios with phenology have lower errors, with the AGDD-PHENO scenario achieving slightly higher accuracy with an RMSE of  $0.85 \text{ m}^2 \text{ m}^{-2}$  (nRMSE 31.25%, NMAD  $0.09 \text{ m}^2 \text{ m}^{-2}$ ) than AGDD-S2-PHENO, where the RMSE is  $0.87 \text{ m}^2 \text{ m}^{-2}$  (nRMSE 31.89%, NMAD  $0.08 \text{ m}^2 \text{ m}^{-2}$ ). In all three cases, modeled GLAI was able to explain between 77 (NO-PHENO) and 84% (AGDD-PHENO and AGDD-S2-PHENO) of the variance in the in-situ data.

The higher overall accuracy is mainly due to the first phenological phase (GE-ET), in which the RMSE decreases from  $0.6 \text{ m}^2 \text{ m}^{-2}$  (nRMSE 217.52%) in the case of NO-PHENO to  $0.16 \text{ m}^2 \text{ m}^{-2}$  (nRMSE: 58.04%) in the AGDD-PHENO setup (N=42). We assume the increase in retrieval accuracy was mainly due to optimization in the inversion setup (see Table 6): When using a larger LUT and a higher number of solutions, the retrieval error increased to  $> 100\%$ . The ill-posedness of RTM inversion, however, makes it difficult to make a conclusive statement. Without optimizing the inversion setup, the retrieval error was up to 100%. In the SE-EH macro stage, the NO-PHENO scenario is slightly better than the AGDD-PHENO scenario with an RMSE of  $0.88 \text{ m}^2 \text{ m}^{-2}$  and  $0.95 \text{ m}^2 \text{ m}^{-2}$ , respectively (relative errors: 22.08% and 23.75%, N=67). In the last phenological macro stage, both models performed similar with an RMSE of  $1.07 \text{ m}^2 \text{ m}^{-2}$  (relative error: 23.1%, N=39). In these two stages, the RTM inversion setup was the same for both approaches as suggested by the systematic optimization approach.

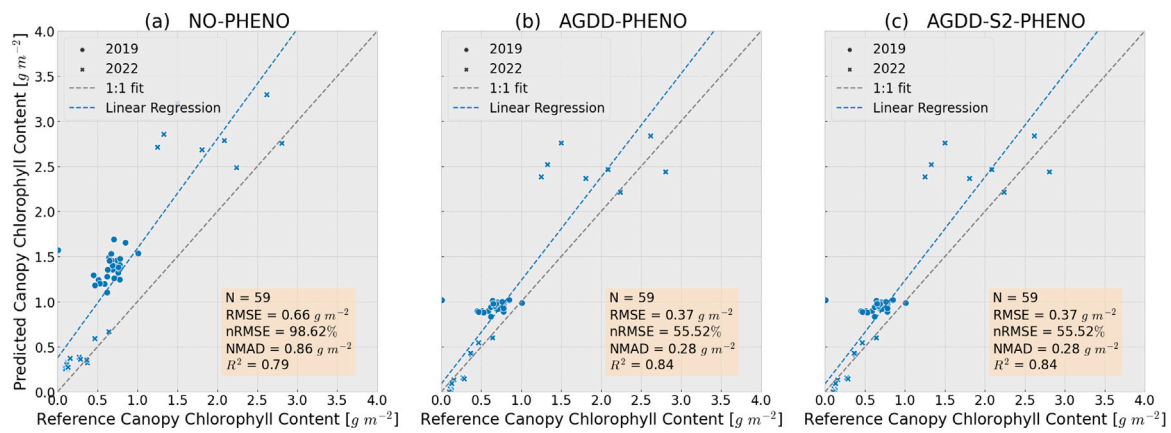


Fig. 6. Scatter plots between in-situ reference and RTM-derived CCC for the NO-PHENO (a), AGDD-PHENO (b), and AGDD-S2-PHENO (c) scenario setups. The year the data was collected is denoted by dots (2019) and crosses (2022).

#### 4.2.2. Canopy chlorophyll content

As with GLAI, the incorporation of phenology shows an increase in the accuracy of CCC retrieval. Unfortunately, fewer data points ( $N=59$ ) are available for validation of CCC. Also, these are limited to the early growth stages (GE-ET and SE-EH). Fig. 6 shows the in-situ measured versus modeled CCC. The RMSE of CCC retrieval is about  $0.37\ g\ m^{-2}$  (nRMSE: 55.52%, NMAD:  $0.28\ g\ m^{-2}$ ) in the two phenological setups versus an RMSE of  $0.66\ g\ m^{-2}$  (nRMSE 98.62%, NMAD:  $0.86\ g\ m^{-2}$ ) in the NO-PHENO baseline. The modeled CCC explained between 79 and 84% of the variance in the in situ values. When looking at the 2019 data alone ( $N=29$ , see cross markers in Fig. 6), an extremely poor retrieval performance can be observed with an  $R^2$  of around 0.02. AGDD-PHENO and AGDD-S2-PHENO (Fig. 6b, c) show the same retrieval accuracy as the data only includes data points for which both models agreed on the same phenological macro stage.

#### 4.2.3. Spatio-temporal considerations

Fig. 7 shows maps of modeled GLAI (top row), CCC (middle row), and Cab (bottom row) for selected S2 scenes in 2022 for the Witzwil site (Parzelle 35) depicting all three phenological macro stages. Traits are based on the AGDD-PHENO scenario which outperformed the other two setups in terms of trait retrieval accuracy. Fig. 7 shows the high correlation between GLAI and CCC when comparing them on a pixel-by-pixel basis ( $R^2$  between 0.97 and 0.99,  $N=2604$  pixels per S2 scene). The correlation between GLAI and Cab is more variable and shows a change over the season: for example,  $R^2$  is 0.5 at the beginning of stem elongation (20220325, second column from left in Fig. 7) and increases to 0.91 at the last date shown (20220618, right column in Fig. 7). An increase of trait values starting in March (GE-ET) towards a maximum in May (FL-PM) can be observed (second column from the right in Fig. 7) followed by a decrease in the last S2 scene (right column in Fig. 7) at the onset of senescence. A clear spatial pattern is visible in the field (upper central part), which can be explained by soil subsidence and associated water logging (Egli et al., 2020). The observed field heterogeneity coincides with the experience of the local farmer. The spatial patterns are similar in all three traits.

Maps for the other field parcels studied in 2022 showing the same calendar dates can be found in the Appendix A (Figures A.10–A.15). Moreover, a map of GLAI, CCC, and Cab for April 20th, 2019 is shown in Figure A.9 for the two field parcels at which different nitrogen treatments were applied (see Section 2.2).

The high correlation between modeled GLAI and CCC applies to all field parcels and S2 scenes in 2022. The correlation between GLAI and Cab is weaker overall. It shows a seasonal change from low correlation in tillering and beginning of stem elongation to high correlation after ear swelling (BBCH macro stage 40). In 2019, the aforementioned poor retrieval accuracy in GLAI and CCC resulted in lower correlation

between modeled GLAI and CCC ( $R^2$  around 0.73). This is lower than in the independent calibration dataset (see Section 3.3 and Fig. 2).

Fig. 8 shows median GLAI (top row), CCC (middle row), and Cab (lower row) trajectories derived from the AGDD-PHENO scenario for all field parcels investigated in 2022. Median trait values are plotted per S2 image acquisition date in calendar dates (Fig. 8, a) and AGDD (Fig. 8, b). For all fields, the traits follow plausible temporal patterns. GLAI values increase steadily from  $< 1\ m^2\ m^{-2}$  at the beginning of March (GE-ET phase) and reach a maximum in early summer (4 to  $5.5\ m^2\ m^{-2}$ ), followed by a decline in the FL-PM phase reaching values around  $1\ m^2\ m^{-2}$  in mid and late July. CCC closely follows the seasonal trajectory of GLAI (Fig. 8, middle row). Cab (Fig. 8, lower row) reveals a slightly different picture: Cab values start to increase earlier than GLAI and show only a slight decline towards the end of the season. This means, the same GLAI value (e.g.,  $1\ m^2\ m^{-2}$ ) at the start and end of the season has different Cab levels: Lower Cab levels ( $< 40\ \mu g\ cm^{-2}$ ) at the beginning of the season (around AGDD 700 to 800 °C) and higher Cab levels ( $>= 40\ \mu g\ cm^{-2}$ ) during the last phenological macro stage (FL-PM, around AGDD 2200 to 2500 °C).

By comparing calendar dates and AGDDs, some interesting observations can be made: The GLAI of the organically managed Broatefaeld plot (Arenenberg site, see Table 2) is lower than the GLAI of the other fields and shows a delayed increase of the GLAI in the AGDD scale. Cab levels, however, are similar to the other parcels. In case of Parzelle 35 (Witzwil site) there is an earlier increase of GLAI with respect to calendar dates. However, in the AGDD scale, it can be seen that the wheat in this field lags behind the other fields except for the aforementioned Broatefaeld parcel and also requires a much higher cumulative temperature sum ( $\sim 2700\ ^\circ C\ d$ ) to reach maturity. The other six fields already reach this value around AGDD 2200. Notably, in the calendar view, all fields reach these low GLAI values at almost the same time by mid of July when harvest took place (between July 15th at Broatefaeld and July 27th at Ruetteli, SwissFutureFarm).

## 5. Discussion

### 5.1. Phenological macro stages

The AGDD-PHENO scenario based on AGDD demonstrates that the results obtained from observing the physiological changes in winter wheat in small-scale field phenotyping sites can be applied to larger agricultural systems at the landscape scale. This means that it is possible to upscale the findings. We assert that by combining physically-based models (RTMs) with prior knowledge of physiology and phenology, we are able to accurately encode the essential physical and biological principles needed for the transfer of information across space and time at the landscape scale.

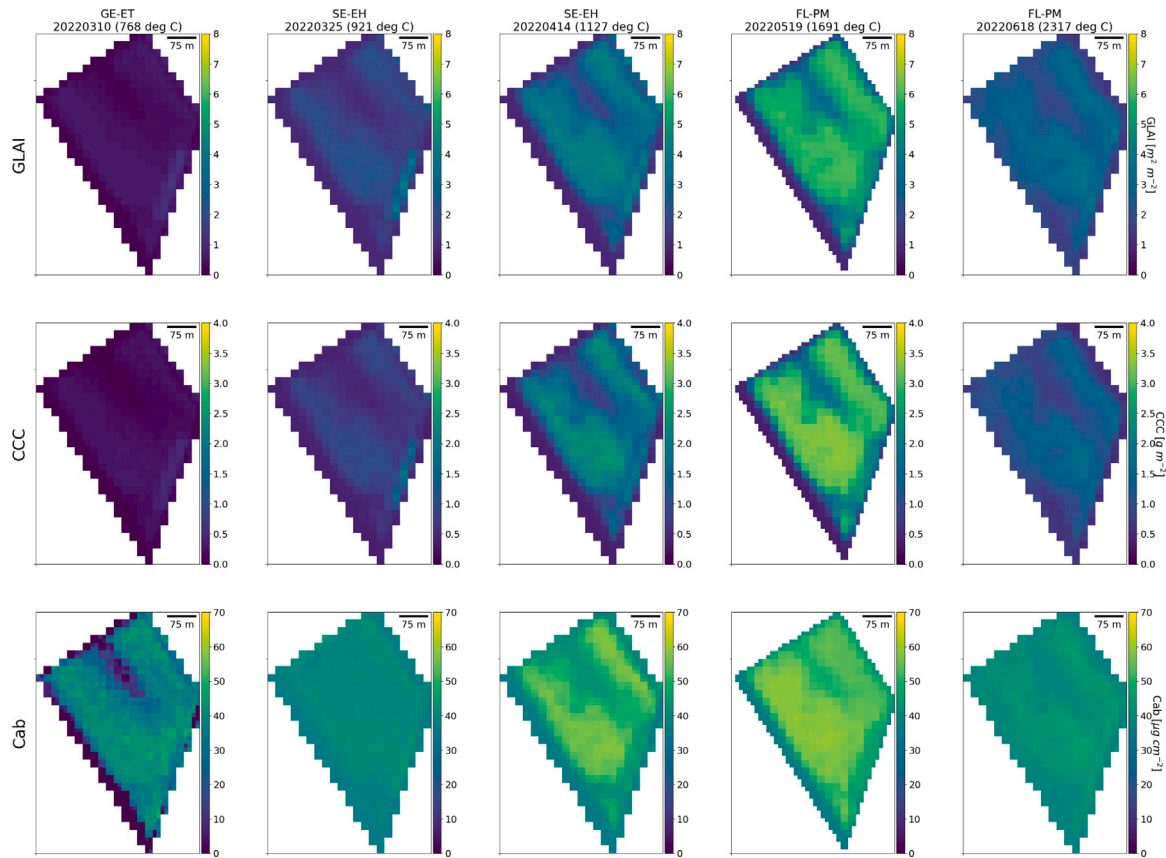


Fig. 7. Maps of GLAI (top), CCC (middle), and Cab (bottom) derived from the best performing scenario (PHENO-AGDD) for Witzil (Parzelle 35). The maps are obtained from selected S2 overpasses depicting the three phenological macro stages of winter wheat (AGDD in brackets).

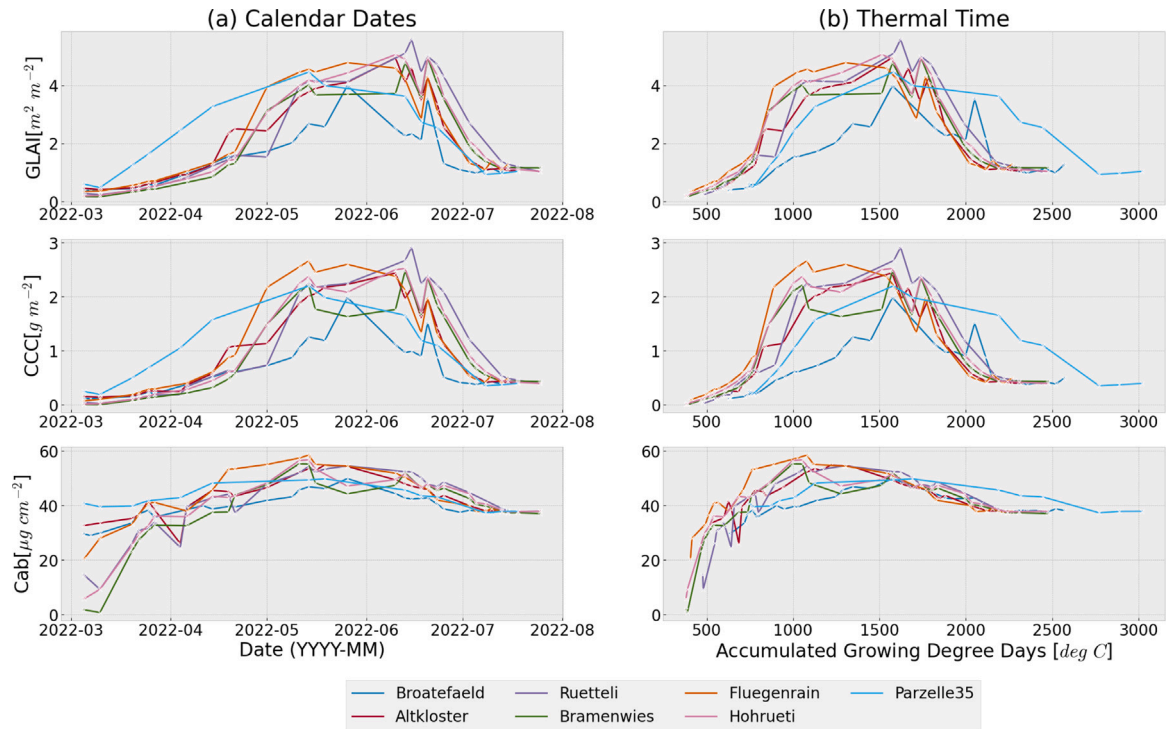


Fig. 8. Trajectories of median GLAI (top row), CCC (middle row), Cab (lower row) values per field parcel with x-axis plotted in calendar dates (a) (i.e., S2 image acquisition dates) and accumulated growing degree days (b).

Due to the dependence on temperature sums, the approach works in real-time during the season (first research question). Thanks to its simplicity the proposed approach can be easily adopted for operational usage since only basic weather station or gridded meteorological data is required. Information on exact occurrence of phenological transition, however, is not provided. Given the inherent uncertainty in S2 (Graf et al., 2023) and temperature data, determining transitions with high precision (e.g., up to single days) is not considered useful as uncertainty alone might be in the range of a couple of days. Our approach also does not allow a more fine-grained view on phenology, such as the onset of tillering (BBCH 21) or booting (BBCH 41). This is, however, mainly to lack of corresponding phenological ratings. As Liao et al. (2023) showed the detection of further phenological macro stages from remotely-sensed data is possible given calibration data availability.

Our approach differs substantially from previous remote sensing studies of phenology, which are mostly based on time series analyses of growing seasons that have already been completed (Zeng et al., 2020). Phenology estimates in real time are therefore often not possible. In addition, we circumvent the need to fit a time series to remotely sensed data points, which is associated with large uncertainties and potential for error (Younes et al., 2021). Especially in geographic regions with high annual cloud cover such as the mid-latitudes or tropical regions, fitting of time series can fail or lead to implausible estimates of phenology. Furthermore, our approach models phenology as stages with physiological significance, which is often not fully addressed in remote sensing studies and limits their interpretability as well as applicability to agriculture.

The AGDD scenarios may encounter limitations when temperature is not the main driving factor for phenological development (e.g., under water-limited conditions), or when crops are stressed in some other ways (Bönecke et al., 2020). Mechanistic crop growth models might therefore be a more sophisticated and reliable alternative. Moreover, the AGDD-PHENO scenario cannot detect differences in phenology within the field as we have a single temperature reading per field. This was the motivation for adding the cost function value from the RTM inversion (AGDD-S2-PHENO) to introduce spatial detail from remote sensing. This scenario revealed slightly lower accuracy (Table 8). Still, due to the small number ( $N = 31$ ) of S2 observations with corresponding in-situ BBCH ratings at the critical AGDD windows (see Section 4.1), it is difficult to make conclusive assessments. Arguably, canopy structure might only change gradually during the transition from one phenological stage to the other and so might the influence on the spectral properties. Consequently, slight uncertainties in determining the phenological stage will have limited effect on the trait retrieval. As Liao et al. (2023) showed that spectral information from S2 data can indeed be used to reveal spatial differences in phenological macro stages within wheat fields, we still see great potential in this approach. However, a more conclusive metric than the value of the cost function of the RTM inversion needs to be found.

The AGDD windows based on multi-year field phenotyping and a large number of genotypes are valid for Swiss conditions and those of neighboring western and central European countries due to European GABI wheat panel (see Section 2.1.1) and similar environmental conditions in terms of climate and soils. It should be noted that breeding progress, for example towards climate-resilient varieties, may require recalibration in the future. On the example of wheat cultivars in Western Germany between 1952 and 2013, Rezaei et al. (2018) showed that historical changes in wheat phenology are mainly due to breeding progress, as modern cultivars require a lower temperature sum to reach flowering. However, this is only feasible if sufficient data from field phenotyping from multiple years and geographic locations is available. The same applies regarding the transferability of our approach to other important crops such as maize or soybean or future climate conditions.

## 5.2. Functional trait retrieval

The usage of field phenotyping data improved RTM-based functional trait retrieval (second research question).

### 5.2.1. Retrieval accuracy

Seasonal trajectories of GLAI, CCC, and Cab showed meaningful patterns (Fig. 8) and reflected large-scale field heterogeneity (Fig. 7). The use of thermal time as a complement to calendar dates also creates the basis for making plant growth and phenology comparable in space and time, since temperature sums represent a common frame of reference. In the 2019 N-experiment, in which field heterogeneity was artificially increased the models showed poor performance and were not able to resolve small-scale field heterogeneity. We attribute this issue to two main causes: First, the plot design of the experiment might still be too small compared to the spatial resolution of S2 (see Section 2.2). Second, the GLAI-CCC relationship (see Fig. 2) used as physiological prior to calibrate the models was not obtained under field conditions under which small-scale heterogeneity was exaggerated artificially. Thus, more calibration data might be required to enable a more accurate retrieval of CCC under variable field management conditions.

The relationship between GLAI and Cab shows decoupling at early growth stages (see Figs. 7 and 8). This is plausible, since large fluctuations in Cab are to be expected at low biomass values in the vegetative phase (Lemaire et al., 2008). The same applies to the senescence phase (BBCH > 90). For senescence, unfortunately, we have no validation data (see Section 3.5) and only few calibration data, since the distinction between green and brown, i.e., photosynthetically inactive, LAI is a highly subjective task. Therefore, further calibration and validation data are needed to model and validate senescence.

It is also important to consider that the inversion result arises from the aggregation of several solutions, using the entire spectral information. This can cause variations in the chlorophyll content to disappear: First, the inversion is more sensitive to changes in GLAI, as GLAI - unlike chlorophyll - affects all spectral bands (Verrelst and Rivera, 2017). Second, the aggregation by using the median of the  $n$  best solutions might suppress small leaf chlorophyll variations similarly to noise.

Generally, the retrieval accuracy of functional traits is between values found in studies using S2 data and PROSAIL simulations: For example, Xie et al. (2019) obtained an RMSE in GLAI of  $1.53 \text{ m}^2 \text{ m}^{-2}$  for winter wheat, while Pan et al. (2019) reported an RMSE of  $0.43 \text{ m}^2 \text{ m}^{-2}$  (nRMSE: 11%), both in Northern China. Using a multi-year dataset obtained on wheat fields in Belgium, Delloye et al. (2018) reported RMSE about  $0.7 \text{ m}^2 \text{ m}^{-2}$  (nRMSE: 35.86%) when using the S2 red-edge bands for RTM inversion, which was similar to the error we obtained from all bands (RMSE:  $0.72 \text{ m}^2 \text{ m}^{-2}$ ). For CCC, an error of  $0.35 \text{ gm}^{-2}$  was obtained from all S2 bands resulting in a relative error of 26.37%. In a multi-crop approach on winter wheat and maize in Southern Germany (Estévez et al., 2021) reported an RMSE of  $0.48 \text{ m}^2 \text{ m}^{-2}$  (nRMSE: 12.94%) in GLAI and of  $0.39 \text{ gm}^{-2}$  in CCC (nRMSE: 18.14%). However, their sample size is small ( $N=14$ ) and only includes three winter wheat samples.

Notably, none of the aforementioned studies used physiological or phenological priors from field phenotyping as suggested in this study. One might therefore conclude that similar retrieval accuracy can be achieved without the explicit usage of field phenotyping data. However, only in few studies, e.g., by Delloye et al. (2018), GLAI and CCC were derived simultaneously, making direct comparisons to our work difficult. Moreover, only in few cases have the data used been disclosed, so we could not directly compare our method with those of other authors.

Our findings regarding trait retrieval accuracy might also mean that one-dimensional RTMs such as PROSAIL building on the turbid medium assumption (Verhoef, 1984) have reached their accuracy limit. Turbid medium RTMs represent a canopy as a single layer with absorbing and scattering particles dissolved uniformly in it. Thus, the alignment of leaves in vertically-structured layers with different optical properties found in winter wheat cannot be fully represented (Zhao et al., 2017). Significant changes in trait retrieval accuracy might only be possible

using more sophisticated models, such as RTMs with multiple leaf layers (Verhoef and Bach, 2007) or three-dimensional RTMs (Jiang et al., 2022). To do so, the incorporation of further structural and morphological traits such as leaf angles or the vertical distribution of leaves in plants from field phenotyping might be beneficial. Advancing the development of RTMs towards a higher degree of morphological and physiological plausibility were, however, beyond the scope of this study.

### 5.2.2. The role of phenology

The incorporation of phenology increased trait retrieval accuracy. This is especially due to the possibility to optimize the RTM inversion setup for the individual stages, i.e., to optimize the size of the LUT, number of solutions and choice of cost function per phenological macro stage. Our experiments suggest that optimizing the inversion configuration has a greater influence than the actual phenological priors (see Section 4.2). These findings are consistent with previous studies about RTM inversion, e.g., by Verrelst et al. (2014). Moreover, it seems conceivable to adjust the selection of spectral channels per phenological stage, since the sensitivity of spectral channels to GLAI and CCC depends on the phenological developmental stage: For instance, at low LAI values, the sensitivity to a leaf trait such as Cab is weak (Verhoef et al., 2018).

Furthermore, our approach allows to consider different traits per phenological macro stage or to parameterize them with greater attention. This is possible because the macro stages represent important physiological transitions in winter wheat, in which different traits are important to study. For example, during the first stage (GE-ET), green canopy cover is a trait of great relevance. Canopy cover is used to quantify, e.g., the interception of radiation (Steven et al., 1986) or to determine the risk of soil erosion by water (Gabriels et al., 2003). Thus, in further research, this trait could be modeled for this phenological macro stage.

### 5.2.3. An up-scaling problem?

The strength of the linear relationship between modeled GLAI and CCC is either higher (2022 data, Fig. 7) or lower (2019) than suggested by the multi-year phenotyping data (Fig. 2). Seemingly, the remotely sensed GLAI-CCC relationship is over-simplified. This reveals a fundamental problem in the derivation of CCC from S2 imagery. While CCC is conceptually a canopy trait, it is directly related to leaf chlorophyll and thus to the leaf scale. Therefore, in-situ measurement and RTM-based estimation of CCC always requires up-scaling, since only the leaf trait can be measured or modeled. In addition, for both in-situ and RTM CCC determination, it is assumed that chlorophyll is distributed uniformly in the canopy. This assumption ignores that chlorophyll content tends to decrease from the top of the canopy towards the ground due to vertical distribution of leaves in wheat (Huang et al., 2011) - which again might call for more complex RTMs.

There is also the question of an appropriate scheme for in-situ sampling of a leaf trait (Cab) for up-scaling to the canopy (i.e., CCC). If only leaves from the upper leaf level are taken, this might intuitively come closer to what the satellite sees, which ultimately measures the top-of-canopy reflectance. However, this is not representative of the entirety of the canopy as previously explained. Moreover, since the entire canopy contributes to the total reflectance (Kuusk, 1995; Wang and Li, 2013; D'Odorico et al., 2018), albeit decreasing with distance from the canopy surface, an in-situ leaf sample should also include leaves from lower tiers. Arguably, this topic deserves more attention and should be addressed by further research.

### 5.3. Advancing agricultural remote sensing

By using priors from field phenotyping such as correlations between traits (see Section 3.3) and concepts such as growing degree days or

the BBCH scale our results are physiologically sound, physically-based and can be interpreted by agronomist and stakeholders in agriculture. In-season crop assessment on large scale plays a crucial role in global food security by providing early warning systems (Becker-Reshef et al., 2020). The approach presented can be integrated into existing process-based crop growth models in many of which GLAI is a key state variable (Delécolle et al., 1992). Further, improved assessment of crop growth can be used on a local scale by practitioners. Many precision farming applications rely on remotely sensed data to, e.g., determine the plant fertilization demand (Argento et al., 2021, 2022). Thus, improving the plant trait retrieval arguably enhances the accuracy and efficiency of precision agriculture tools. With our approach, we mitigate overcome shortcomings identified in the remote sensing literature by adding a tool to the toolbox of remote sensing that offers improvement of data and enhanced interpretability. This opens opportunities for further interdisciplinary research and will arguably advance agricultural remote sensing.

Again, our approach is arguably simple and requires only basic weather station data. Thus, it is suited for operational usage and can be applied on large spatial scales. In the same way, our approach could be transferred to other crops given that field phenotyping data is available to constrain the modeling of growth and phenology. Further research could address enhancements in RTMs, and focus on more advanced modeling of crop growth and phenology, e.g., by including dose-response relationships (Roth et al., 2021, 2022b) and process-based crop models.

## 6. Conclusions

Bringing together field phenotyping and remote sensing opens unprecedented opportunities to deepen our understanding of crop growth and development. We showed that insights from field phenotyping can be used to monitor winter wheat growth and phenological macro stages on the landscape scale by RTM inversion on S2 imagery. The proposed approach works in near real-time and thus meets the requirements for many agricultural applications, such as fertilizer and pesticide scheduling. The use of phenological and physiological priors using multi-year field phenotyping data improved RTM-based trait retrieval accuracy and paves the way for improving RTM parametrization and the selection of traits according to physiological considerations and environmental covariates. In terms of phenological macro stages, we demonstrated that accumulated temperature sums from field phenotyping experiments could be used to identify the three main phenological macro stages in wheat using S2 imagery. These macro stages have a physiological meaning and are therefore an improvement compared to many previous remote sensing attempts to phenology. Our work enables physiologically sound comparisons between sites and wheat cultivars which is important to study plant-environment interactions at the landscape scale.

Further research should address open points regarding the up-scaling of leaf traits to the canopy and the collection of further calibration and validation data. In addition, more attention should be paid to a more fine-grained view on phenology. Furthermore, phenological stages for which little data are currently available such as senescence should be studied in greater detail. We also see a need for more advanced canopy RTMs, which should account for vertical and horizontal gradients in canopies in terms of leaf distribution and morphology.

### CRedit authorship contribution statement

**Lukas Valentin Graf:** Conceptualization, Methodology, Formal analysis, Validation, Visualization, Software, Writing – original draft. **Quirina Noëmi Merz:** Writing – original draft, Field work, Lab work. **Achim Walter:** Supervision, Review & editing. **Helge Aasen:** Supervision, Review & editing.

## Declaration of competing interest

The authors declare the following financial interests/personal relationships which may be considered as potential competing interests: Lukas Valentin Graf reports financial support was provided by Swiss National Science Foundation. Quirina Noemi Merz reports financial support was provided by Swiss National Science Foundation.

## Data availability

Code to reproduce the entire workflow including calibration and validation data is available at [https://github.com/EOA-team/sentinel2\\_crop\\_traits](https://github.com/EOA-team/sentinel2_crop_traits) under GNU General Public License v3.0.

## Acknowledgments

LVG acknowledges funding of the Swiss National Science Foundation for the project “PhenomEn” (grant number IZCOZ0\_198091). QNM’s work is supported by the Swiss National Science Foundation, within the framework of the National Research Programme “Sustainable Economy: resource-friendly, future-oriented, innovative” (NRP 73), in the InnoFarm project, Grant-N° 407340\_172433. We thank Bernhard Streit and Alfred Burri for providing access and resources at the Witzwil site, Marco Landis for his support at Strickhof, Florian Abt at Arenenberg and Thomas Anken and his team for their support at the Swiss Future Farm. Furthermore, we thank the field technicians - namely Hansulrich Zbinden, Katharina Casada and Matthias Hatt - at Agroscope Reckenholz and Agroscope Taenikon for their invaluable support in the field and laboratory. We are thankful to our student assistants - namely Lara Wyser, Finn Timcke, Bérénice Goin, Dea Spiess, Rike Teuber, and Jania Mackenthun - for their support in the field. Furthermore, we have to thank Francesco Argento, Agroscope Reckenholz, for providing access to in-situ data. Special thanks go to Samuel Wildhaber, who contributed significantly to the development of the GLAI measurement protocol and supported the field work. Last, we thank the Group of Crop Science at ETH and in particular Lukas Roth, Lukas Kronenberg, Flavian Tschurr, and Olivia Zumsteg for providing phenology data as well as Norbert Kirchgessner for his support in data processing and storage.

## Appendix A. Supplementary data

Supplementary material related to this article can be found online at <https://doi.org/10.1016/j.rse.2023.113860>.

## References

Aasen, H., Roth, L., 2022. Advances in high-throughput crop phenotyping using unmanned aerial vehicles (UAVs). In: Walter, A. (Ed.), *Burleigh Dodds Series in Agricultural Science*. Burleigh Dodds Science Publishing, pp. 179–200. <http://dx.doi.org/10.19103/AS.2022.0102.09>, URL <https://shop.bdsublishing.com/store/bds/detail/product/3-190-9781801465298>.

Araus, J.L., Cairns, J.E., 2014. Field high-throughput phenotyping: the new crop breeding frontier. *Trends Plant Sci.* 19 (1), 52–61. <http://dx.doi.org/10.1016/j.tplants.2013.09.008>, URL <https://www.sciencedirect.com/science/article/pii/S1360138513001994>.

Argento, F., Anken, T., Abt, F., Vogelsanger, E., Walter, A., Liebisch, F., 2021. Site-specific nitrogen management in winter wheat supported by low-altitude remote sensing and soil data. *Precis. Agric.* 22 (2), 364–386. <http://dx.doi.org/10.1007/s11119-020-09733-3>.

Argento, F., Liebisch, F., Anken, T., Walter, A., El Benni, N., 2022. Investigating two solutions to balance revenues and N surplus in Swiss winter wheat. *Agric. Syst.* 201, 103451. <http://dx.doi.org/10.1016/j.agsy.2022.103451>, URL <https://www.sciencedirect.com/science/article/pii/S0308521X22000877>.

Atzberger, C., 2004. Object-based retrieval of biophysical canopy variables using artificial neural nets and radiative transfer models. *Remote Sens. Environ.* 93 (1), 53–67. <http://dx.doi.org/10.1016/j.rse.2004.06.016>, URL <https://www.sciencedirect.com/science/article/pii/S0034425704001956>.

Bach, H., Mauser, W., 2018. Sustainable Agriculture and Smart Farming. In: Mathieu, P.-P., Aubrecht, C. (Eds.), *Earth Observation Open Science and Innovation*. In: ISSI Scientific Report Series, Springer International Publishing, pp. 261–269. [http://dx.doi.org/10.1007/978-3-319-65633-5\\_12](http://dx.doi.org/10.1007/978-3-319-65633-5_12).

Becker-Reshef, I., Justice, C., Barker, B., Humber, M., Rembold, F., Bonifacio, R., Zappacosta, M., Budde, M., Magadzire, T., Shitote, C., Pound, J., Constantino, A., Nakalembe, C., Mwangi, K., Sobue, S., Newby, T., Whitcraft, A., Jarvis, I., Verdin, J., 2020. Strengthening agricultural decisions in countries at risk of food insecurity: The GEOGLAM crop monitor for early warning. *Remote Sens. Environ.* 237, 111553. <http://dx.doi.org/10.1016/j.rse.2019.111553>, URL <https://www.sciencedirect.com/science/article/pii/S0034425719305735>.

de Beurs, K.M., Henebry, G.M., 2004. Land surface phenology, climatic variation, and institutional change: Analyzing agricultural land cover change in Kazakhstan. *Remote Sens. Environ.* 89 (4), 497–509. <http://dx.doi.org/10.1016/j.rse.2003.11.006>, URL <https://linkinghub.elsevier.com/retrieve/pii/S0034425703003432>.

Bolton, D.K., Gray, J.M., Melaas, E.K., Moon, M., Eklundh, L., Friedl, M.A., 2020. Continental-scale land surface phenology from harmonized Landsat 8 and Sentinel-2 imagery. *Remote Sens. Environ.* 240, 111685. <http://dx.doi.org/10.1016/j.rse.2020.111685>, URL <https://linkinghub.elsevier.com/retrieve/pii/S0034425720300547>.

Bönecke, E., Breitsameter, L., Brüggemann, N., Chen, T.-W., Feike, T., Kage, H., Kersebaum, K.-C., Piepho, H.-P., Stützel, H., 2020. Decoupling of impact factors reveals the response of German winter wheat yields to climatic changes. *Global Change Biol.* 26 (6), 3601–3626. <http://dx.doi.org/10.1111/gcb.15073>, URL <https://onlinelibrary.wiley.com/doi/10.1111/gcb.15073>.

Chen, Z., Jia, K., Wei, X., Liu, Y., Zhan, Y., Xia, M., Yao, Y., Zhang, X., 2022. Improving leaf area index estimation accuracy of wheat by involving leaf chlorophyll content information. *Comput. Electron. Agric.* 196, 106902. <http://dx.doi.org/10.1016/j.compag.2022.106902>, URL <https://linkinghub.elsevier.com/retrieve/pii/S0168169922002198>.

Chen, Y., Zhang, Z., Tao, F., 2018. Improving regional winter wheat yield estimation through assimilation of phenology and leaf area index from remote sensing data. *Eur. J. Agron.* 101, 163–173. <http://dx.doi.org/10.1016/j.eja.2018.09.006>, URL <https://www.sciencedirect.com/science/article/pii/S1161030118305306>.

Combal, B., Baret, F., Weiss, M., Trubuil, A., Mace, D., Pragnere, A., Myneni, R., Knyazikhin, Y., Wang, L., 2002. Retrieval of canopy biophysical variables from bidirectional reflectance Using prior information to solve the ill-posed inverse problem. *Remote Sens. Environ.* 15.

Danner, M., Berger, K., Wocher, M., Mauser, W., Hank, T., 2017. Retrieval of biophysical crop variables from multi-angular canopy spectroscopy. *Remote Sens.* 9 (7), 726. <http://dx.doi.org/10.3390/rs9070726>, URL <https://www.mdpi.com/2072-4292/9/7/726> Number: 7 Publisher: Multidisciplinary Digital Publishing Institute.

Danner, M., Berger, K., Wocher, M., Mauser, W., Hank, T., 2019. Fitted PROSAIL parameterization of leaf inclinations, water content and brown pigment content for winter wheat and maize canopies. *Remote Sens.* 11 (10), 1150. <http://dx.doi.org/10.3390/rs11101150>, URL <https://www.mdpi.com/2072-4292/11/10/1150> Number: 10 Publisher: Multidisciplinary Digital Publishing Institute.

Danner, M., Berger, K., Wocher, M., Mauser, W., Hank, T., 2021. Efficient RTM-based training of machine learning regression algorithms to quantify biophysical & biochemical traits of agricultural crops. *ISPRS J. Photogramm. Remote Sens.* 173, 278–296. <http://dx.doi.org/10.1016/j.isprsjprs.2021.01.017>, URL <https://linkinghub.elsevier.com/retrieve/pii/S092427162100023X>.

Delécolle, R., Maas, S.J., Guéris, M., Baret, F., 1992. Remote sensing and crop production models: present trends. *ISPRS J. Photogramm. Remote Sens.* 47 (2), 145–161. [http://dx.doi.org/10.1016/0924-2716\(92\)90030-D](http://dx.doi.org/10.1016/0924-2716(92)90030-D), URL <https://www.sciencedirect.com/science/article/pii/092427169290030D>.

Delloy, C., Weiss, M., Defourny, P., 2018. Retrieval of the canopy chlorophyll content from Sentinel-2 spectral bands to estimate nitrogen uptake in intensive winter wheat cropping systems. *Remote Sens. Environ.* 216, 245–261. <http://dx.doi.org/10.1016/j.rse.2018.06.037>, URL <https://www.sciencedirect.com/science/article/pii/S0034425718303158>.

D’Odorico, P., Emmel, C., Revill, A., Liebisch, F., Eugster, W., Buchmann, N., D’Odorico, P., Emmel, C., Revill, A., Liebisch, F., Eugster, W., Buchmann, N., 2018. Vertical patterns of photosynthesis and related leaf traits in two contrasting agricultural crops. *Funct. Plant Biol.* 46 (3), 213–227. <http://dx.doi.org/10.1071/FP18061>, URL <https://www.publish.csiro.au/fp/FP18061> Publisher: CSIRO PUBLISHING.

Egli, M., Gärtner, H., Rössli, C., Seibert, J., Wiesenberg, G.L.B., Wingate, V., 2020. Landschaftsdynamik im Gebiet des Grossen Mooses - Moorböden, Wassermanagement und landwirtschaftliche Nutzung im Spannungsfeld zwischen Produktivität und Nachhaltigkeit. *Schriftenreihe Physische Geogr.* 68, <http://dx.doi.org/10.5167/uzh-190633>, URL <https://www.zora.uzh.ch/id/eprint/190633/> ISBN: 9783906894164 Num Pages: 91 Place: Zürich Publisher: Geographisches Institut der Universität Zürich.

Estévez, J., Berger, K., Vicent, J., Rivera-Caicedo, J.P., Wocher, M., Verrelst, J., 2021. Top-of-atmosphere retrieval of multiple crop traits using variational heteroscedastic gaussian processes within a hybrid workflow. p. 26.

Federal Statistical Office, FSO, 2022. Landwirtschaft und Ernährung - Taschenstatistik 2022 | Publikation. Bundesamt für Statistik URL <https://www.bfs.admin.ch/asset/de/22906536>.

- Féret, J.-B., Gitelson, A., Noble, S., Jacquemoud, S., 2017. PROSPECT-D: Towards modeling leaf optical properties through a complete lifecycle. *Remote Sens. Environ.* 193, 204–215. <http://dx.doi.org/10.1016/j.rse.2017.03.004>, URL <https://linkinghub.elsevier.com/retrieve/pii/S0034425717300962>.
- Frampton, W.J., Dash, J., Watmough, G., Milton, E.J., 2013. Evaluating the capabilities of Sentinel-2 for quantitative estimation of biophysical variables in vegetation. *ISPRS J. Photogramm. Remote Sens.* 82, 83–92. <http://dx.doi.org/10.1016/j.isprsjprs.2013.04.007>, URL <https://linkinghub.elsevier.com/retrieve/pii/S092427161300107X>.
- Gabriels, D., Ghekiere, G., Schiettecatte, W., Rottiers, I., 2003. Assessment of USLE cover-management C-factors for 40 crop rotation systems on arable farms in the Kemmelbeek watershed, Belgium. *Soil Tillage Res.* 74 (1), 47–53. [http://dx.doi.org/10.1016/S0167-1987\(03\)00092-8](http://dx.doi.org/10.1016/S0167-1987(03)00092-8), URL <https://www.sciencedirect.com/science/article/pii/S0167198703000928>.
- Garonna, I., de Jong, R., Schaepman, M.E., 2016. Variability and evolution of global land surface phenology over the past three decades (1982–2012). *Global Change Biol.* 22 (4), 1456–1468. <http://dx.doi.org/10.1111/gcb.13168>, URL <https://onlinelibrary.wiley.com/doi/abs/10.1111/gcb.13168> eprint: <https://onlinelibrary.wiley.com/doi/pdf/10.1111/gcb.13168>.
- Gitelson, A.A., Peng, Y., Arkebauer, T.J., Schepers, J., 2014. Relationships between gross primary production, green LAI, and canopy chlorophyll content in maize: Implications for remote sensing of primary production. *Remote Sens. Environ.* 144, 65–72. <http://dx.doi.org/10.1016/j.rse.2014.01.004>, URL <https://www.sciencedirect.com/science/article/pii/S0034425714000170>.
- Gitelson, A.A., Viña, A., Arkebauer, T.J., Rundquist, D.C., Keydan, G., Leavitt, B., 2003. Remote estimation of leaf area index and green leaf biomass in maize canopies. *Geophys. Res. Lett.* 30 (5), <http://dx.doi.org/10.1029/2002GL016450>, URL <https://onlinelibrary.wiley.com/doi/abs/10.1029/2002GL016450> eprint: <https://onlinelibrary.wiley.com/doi/pdf/10.1029/2002GL016450>.
- Gitelson, A.A., Viña, A., Ciganda, V., Rundquist, D.C., Arkebauer, T.J., 2005. Remote estimation of canopy chlorophyll content in crops. *Geophys. Res. Lett.* 32 (8), <http://dx.doi.org/10.1029/2005GL022688>, URL <https://onlinelibrary.wiley.com/doi/abs/10.1029/2005GL022688> eprint: <https://onlinelibrary.wiley.com/doi/pdf/10.1029/2005GL022688>.
- Gitelson, A., Viña, A., Inoue, Y., Arkebauer, T., Schlemmer, M., Schepers, J., 2022. Uncertainty in the evaluation of photosynthetic canopy traits using the green leaf area index. *Agricult. Forest Meteorol.* 320, 108955. <http://dx.doi.org/10.1016/j.agrformet.2022.108955>, URL <https://www.sciencedirect.com/science/article/pii/S0168192322001459>.
- Gogna, A., Schulthess, A.W., Röder, M.S., Ganal, M.W., Reif, J.C., 2022. Gabi wheat a panel of European elite lines as central stock for wheat genetic research. *Sci. Data* 9 (1), 538. <http://dx.doi.org/10.1038/s41597-022-01651-5>, URL <https://www.nature.com/articles/s41597-022-01651-5> Number: 1 Publisher: Nature Publishing Group.
- González, F.G., Slafer, G.A., Miralles, D.J., 2003. Grain and floret number in response to photoperiod during stem elongation in fully and slightly vernalized wheats. *Field Crops Res.* 81 (1), 17–27. [http://dx.doi.org/10.1016/S0378-4290\(02\)00195-8](http://dx.doi.org/10.1016/S0378-4290(02)00195-8), URL <https://www.sciencedirect.com/science/article/pii/S0378429002001958>.
- Graf, L.V., Gorroño, J., Hueni, A., Walter, A., Aasen, H., 2023. Propagating Sentinel-2 top-of-atmosphere radiometric uncertainty into land surface phenology metrics using a Monte Carlo framework. *IEEE J. Sel. Top. Appl. Earth Obs. Remote Sens.* 1–41. <http://dx.doi.org/10.1109/JSTARS.2023.3297713>.
- Graf, L.V., Perich, G., Aasen, H., 2022. EOdal: An open-source Python package for large-scale agroecological research using earth observation and gridded environmental data. *Comput. Electron. Agric.* 203, 107487. <http://dx.doi.org/10.1016/j.compag.2022.107487>, URL <https://www.sciencedirect.com/science/article/pii/S0168169922007955>.
- Hashimoto, N., Saito, Y., Yamamoto, S., Ishibashi, T., Ito, R., Maki, M., Homma, K., 2022. Feasibility of yield estimation based on leaf area dynamics measurements in rice paddy fields of farmers. *Field Crops Res.* 286, 108609. <http://dx.doi.org/10.1016/j.fcr.2022.108609>, URL <https://www.sciencedirect.com/science/article/pii/S0378429022001800>.
- Hay, R.K.M., Kirby, E.J.M., 1991. Convergence and synchrony—a review of the coordination of development in wheat. *Aust. J. Agric. Res.* 42 (5), 661–700. <http://dx.doi.org/10.1071/ar9910661>, URL <https://www.publish.csiro.au/ar/ar9910661> Publisher: CSIRO PUBLISHING.
- Helman, D., 2018. Land surface phenology: What do we really “see” from space? *Sci. Total Environ.* 618, 665–673. <http://dx.doi.org/10.1016/j.scitotenv.2017.07.237>, URL <https://linkinghub.elsevier.com/retrieve/pii/S004896971731954X>.
- Holman, J.D., Lollato, R.P., Zarnstorff, M., Houx, J., Assefa, Y., 2022. Impact of simulated hail damage at different growth stages and canopy positions on rainfed and irrigated winter wheat. *Agron. J.* n/a (n/a), <http://dx.doi.org/10.1002/aj2.21256>, URL <https://onlinelibrary.wiley.com/doi/abs/10.1002/aj2.21256> eprint: <https://onlinelibrary.wiley.com/doi/pdf/10.1002/aj2.21256>.
- Huang, J., Tian, L., Liang, S., Ma, H., Becker-Reshef, I., Huang, Y., Su, W., Zhang, X., Zhu, D., Wu, W., 2015. Improving winter wheat yield estimation by assimilation of the leaf area index from Landsat TM and MODIS data into the WOFOST model. *Agricult. Forest Meteorol.* 204, 106–121. <http://dx.doi.org/10.1016/j.agrformet.2015.02.001>, URL <https://www.sciencedirect.com/science/article/pii/S0168192315000295>.
- Huang, W., Wang, Z., Huang, L., Lamb, D.W., Ma, Z., Zhang, J., Wang, J., Zhao, C., 2011. Estimation of vertical distribution of chlorophyll concentration by bidirectional canopy reflectance spectra in winter wheat. *Precis. Agric.* 12 (2), 165–178. <http://dx.doi.org/10.1007/s11119-010-9166-5>.
- Jacquemoud, S., Bidet, L., Francois, C., Pavan, G., 2003. ANGERS leaf optical properties database (2003). URL <https://ecosis.org/package/angers-leaf-optical-properties-database--2003->.
- Jacquemoud, S., Verhoef, W., Baret, F., Bacour, C., Zarco-Tejada, P.J., Asner, G.P., François, C., Ustin, S.L., 2009. PROSPECT+SAIL models: A review of use for vegetation characterization. *Remote Sens. Environ.* 113, S56–S66. <http://dx.doi.org/10.1016/j.rse.2008.01.026>, URL <https://www.sciencedirect.com/science/article/pii/S0034425709000765>.
- Jiang, J., Weiss, M., Liu, S., Baret, F., 2022. Effective GAI is best estimated from reflectance observations as compared to GAI and LAI: Demonstration for wheat and maize crops based on 3D radiative transfer simulations. *Field Crops Res.* 283, <http://dx.doi.org/10.1016/j.fcr.2022.108538>.
- Kirchgessner, N., Liebisch, F., Yu, K., Pfeifer, J., Friedli, M., Hund, A., Walter, A., 2017. The ETH field phenotyping platform FIP: a cable-suspended multi-sensor system. *Funct. Plant Biol.* 44 (1), 154. <http://dx.doi.org/10.1071/FP16165>, URL <http://www.publish.csiro.au/?paper=FP16165>.
- Körner, C., 2021. Tools Shape Paradigms of Plant-Environment Interactions. In: Cánovas, F.M., Lüttge, U., Risueño, M.C., Pretzsch, H. (Eds.), *Progress in Botany* Vol. 82. Springer International Publishing, Cham, pp. 1–41. [http://dx.doi.org/10.1007/124\\_2020\\_41](http://dx.doi.org/10.1007/124_2020_41).
- Kuusik, A., 1995. A Markov chain model of canopy reflectance. *Agricult. Forest Meteorol.* 76 (3), 221–236. [http://dx.doi.org/10.1016/0168-1923\(94\)02216-7](http://dx.doi.org/10.1016/0168-1923(94)02216-7), URL <https://www.sciencedirect.com/science/article/pii/0168192394022167>.
- Lancashire, P.D., Bleiholder, H., Boom, T.V.D., Langelüddeke, P., Stauss, R., Weber, E., Witzzenberger, A., 1991. A uniform decimal code for growth stages of crops and weeds. *Ann. Appl. Biol.* 119 (3), 561–601. <http://dx.doi.org/10.1111/j.1744-7348.1991.tb04895.x>, URL <https://onlinelibrary.wiley.com/doi/abs/10.1111/j.1744-7348.1991.tb04895.x> eprint: <https://onlinelibrary.wiley.com/doi/pdf/10.1111/j.1744-7348.1991.tb04895.x>.
- Lauvener, C., Baret, F., Hascoët, L., Buis, S., Le Dimet, F.X., 2008. Multitemporal patch ensemble inversion of coupled surface-atmosphere radiative transfer models for land surface characterization. *Remote Sens. Environ.* 112 (3), 851–861. <http://dx.doi.org/10.1016/j.rse.2007.06.027>, URL <https://www.sciencedirect.com/science/article/pii/S0034425707003963>.
- Lemaire, G., Jefferoy, M.H., Gastal, F., 2008. Diagnosis tool for plant and crop N status in vegetative stage: Theory and practices for crop N management. *Eur. J. Agron.* 28 (4), 614–624. <http://dx.doi.org/10.1016/j.eja.2008.01.005>, URL <https://www.sciencedirect.com/science/article/pii/S1161030108000130>.
- Liao, C., Wang, J., Shan, B., Shang, J., Dong, T., He, Y., 2023. Near real-time detection and forecasting of within-field phenology of winter wheat and corn using Sentinel-2 time-series data. *ISPRS J. Photogramm. Remote Sens.* 196, 105–119. <http://dx.doi.org/10.1016/j.isprsjprs.2022.12.025>, URL <https://www.sciencedirect.com/science/article/pii/S0924271622003409>.
- Lichtenthaler, H.K., Buschmann, C., 2001. Chlorophylls and Carotenoids: Measurement and characterization by UV-VIS spectroscopy. *Curr. Protoc. Food Anal. Chem.* 1 (1), F4.3.1–F4.3.8. <http://dx.doi.org/10.1002/0471142913.faf0403s01>, URL <https://onlinelibrary.wiley.com/doi/abs/10.1002/0471142913.faf0403s01> eprint: <https://onlinelibrary.wiley.com/doi/pdf/10.1002/0471142913.faf0403s01>.
- Liebisch, F., Kung, G., Damm, A., Walter, A., 2014. Characterization of crop vitality and resource use efficiency by means of combining imaging spectroscopy based plant traits. In: 2014 6th Workshop on Hyperspectral Image and Signal Processing: Evolution in Remote Sensing. WHISPERS, IEEE, Lausanne, Switzerland, pp. 1–4. <http://dx.doi.org/10.1109/WHISPERS.2014.8077612>, URL <http://ieeexplore.ieee.org/document/8077612/>.
- Lobert, F., Löw, J., Schwieder, M., Gocht, A., Schlund, M., Hostert, P., Erasmi, S., 2023. A deep learning approach for deriving winter wheat phenology from optical and SAR time series at field level. *Remote Sens. Environ.* 298, 113800. <http://dx.doi.org/10.1016/j.rse.2023.113800>, URL <https://linkinghub.elsevier.com/retrieve/pii/S0034425723003516>.
- Machwitz, M., Pieruschka, R., Berger, K., Schlerf, M., Aasen, H., Fahrner, S., Jiménez-Berni, J., Baret, F., Rascher, U., 2021. Bridging the gap between remote sensing and plant phenotyping—Challenges and opportunities for the next generation of sustainable agriculture. *Front. Plant Sci.* 12, 749374. <http://dx.doi.org/10.3389/fpls.2021.749374>, URL <https://www.frontiersin.org/articles/10.3389/fpls.2021.749374/full>.
- McMaster, G., 1997. Growing degree-days: one equation, two interpretations. *Agricult. Forest Meteorol.* 87 (4), 291–300. [http://dx.doi.org/10.1016/S0168-1923\(97\)00027-0](http://dx.doi.org/10.1016/S0168-1923(97)00027-0), URL <https://linkinghub.elsevier.com/retrieve/pii/S0168192397000270>.
- Meroni, M., d’Andrimont, R., Vrieling, A., Fasbender, D., Lemoine, G., Rembold, F., Seguin, L., Verhegghen, A., 2021. Comparing land surface phenology of major European crops as derived from SAR and multispectral data of Sentinel-1 and -2. *Remote Sens. Environ.* 253, 112232. <http://dx.doi.org/10.1016/j.rse.2020.112232>, URL <https://linkinghub.elsevier.com/retrieve/pii/S0034425720306052>.
- Pan, H., Chen, Z., Ren, J., Li, H., Wu, S., 2019. Modeling winter wheat leaf area index and canopy water content with three different approaches using Sentinel-2 multispectral instrument data. *IEEE J. Sel. Top. Appl. Earth Obs. Remote Sens.* 12 (2), 482–492. <http://dx.doi.org/10.1109/JSTARS.2018.2855564>, Conference Name: IEEE Journal of Selected Topics in Applied Earth Observations and Remote Sensing.

- Parent, B., Tardieu, F., 2012. Temperature responses of developmental processes have not been affected by breeding in different ecological areas for 17 crop species. *New Phytol.* 194 (3), 760–774. <http://dx.doi.org/10.1111/j.1469-8137.2012.04086.x>, URL <https://onlinelibrary.wiley.com/doi/10.1111/j.1469-8137.2012.04086.x>.
- Pask, A., Pietragalla, J., Mullan, D., Reynolds, M.P., 2012. Physiological breeding II: a field guide to wheat phenotyping. URL <https://repository.cimmyt.org/handle/10883/1288> Accepted: 2012-02-24T23:09:09Z Publisher: CIMMYT.
- Pedersen, S.M., Lind, K.M., 2017. Precision agriculture – From mapping to site-specific application. In: Pedersen, S.M., Lind, K.M. (Eds.), *Precision Agriculture: Technology and Economic Perspectives*. In: *Progress in Precision Agriculture*, Springer International Publishing, Cham, pp. 1–20. [http://dx.doi.org/10.1007/978-3-319-68715-5\\_1](http://dx.doi.org/10.1007/978-3-319-68715-5_1).
- Peng, D., Zhang, X., Zhang, B., Liu, L., Liu, X., Huete, A.R., Huang, W., Wang, S., Luo, S., Zhang, X., Zhang, H., 2017. Scaling effects on spring phenology detections from MODIS data at multiple spatial resolutions over the contiguous United States. *ISPRS J. Photogramm. Remote Sens.* 132, 185–198. <http://dx.doi.org/10.1016/j.isprsjprs.2017.09.002>, URL <https://linkinghub.elsevier.com/retrieve/pii/S0924271617303027>.
- Rezaei, E.E., Siebert, S., Hüging, H., Ewert, F., 2018. Climate change effect on wheat phenology depends on cultivar change. *Sci. Rep.* 8 (1), 4891. <http://dx.doi.org/10.1038/s41598-018-23101-2>, URL <http://www.nature.com/articles/s41598-018-23101-2>.
- Roth, L., Barendregt, C., Betrix, C.A., Hund, A., Walter, A., 2022a. High-throughput field phenotyping of soybean: Spotting an ideotype. *Remote Sens. Environ.* 269, 112797. <http://dx.doi.org/10.1016/j.rse.2021.112797>, URL <https://linkinghub.elsevier.com/retrieve/pii/S0034425721005174>.
- Roth, L., Piepho, H.P., Hund, A., 2022b. Phenomics data processing: extracting dose-response curve parameters from high-resolution temperature courses and repeated field-based wheat height measurements. *in silico Plants* 4 (1), diac007. <http://dx.doi.org/10.1093/insilicoplants/diac007>.
- Roth, L., Rodríguez-Álvarez, M.X., van Eeuwijk, F., Piepho, H.P., Hund, A., 2021. Phenomics data processing: A plot-level model for repeated measurements to extract the timing of key stages and quantities at defined time points. *Field Crops Res.* 274, 108314. <http://dx.doi.org/10.1016/j.fcr.2021.108314>, URL <https://www.sciencedirect.com/science/article/pii/S0378429021002604>.
- Steven, M.D., Biscoe, P.V., Jaggard, K.W., Paruntu, J., 1986. Foliage cover and radiation interception. *Field Crops Res.* 13, 75–87. [http://dx.doi.org/10.1016/0378-4290\(86\)90012-2](http://dx.doi.org/10.1016/0378-4290(86)90012-2), URL <https://www.sciencedirect.com/science/article/pii/S0378429086900122>.
- van der Velde, M., Biavetti, I., El-Aydam, M., Niemeyer, S., Santini, F., van den Berg, M., 2019. Use and relevance of European Union crop monitoring and yield forecasts. *Agric. Syst.* 168, 224–230. <http://dx.doi.org/10.1016/j.agsy.2018.05.001>, URL <https://www.sciencedirect.com/science/article/pii/S0308521X17310211>.
- Verhoef, W., 1984. Light scattering by leaf layers with application to canopy reflectance modeling: The SAIL model. *Remote Sens. Environ.* 16 (2), 125–141. [http://dx.doi.org/10.1016/0034-4257\(84\)90057-9](http://dx.doi.org/10.1016/0034-4257(84)90057-9), URL <https://www.sciencedirect.com/science/article/pii/S0034425784900579>.
- Verhoef, W., Bach, H., 2007. Coupled soil-leaf-canopy and atmosphere radiative transfer modeling to simulate hyperspectral multi-angular surface reflectance and TOA radiance data. *Remote Sens. Environ.* 109 (2), 166–182. <http://dx.doi.org/10.1016/j.rse.2006.12.013>, URL <https://www.sciencedirect.com/science/article/pii/S0034425707000077>.
- Verhoef, W., van der Tol, C., Middleton, E.M., 2018. Hyperspectral radiative transfer modeling to explore the combined retrieval of biophysical parameters and canopy fluorescence from FLEX – Sentinel-3 tandem mission multi-sensor data. *Remote Sens. Environ.* 204, 942–963. <http://dx.doi.org/10.1016/j.rse.2017.08.006>, URL <https://linkinghub.elsevier.com/retrieve/pii/S0034425717303607>.
- Verrelst, J., Rivera, J., 2017. A global sensitivity analysis toolbox to quantify drivers of vegetation radiative transfer models. In: *Sensitivity Analysis in Earth Observation Modelling*. Elsevier, pp. 319–339. <http://dx.doi.org/10.1016/B978-0-12-803011-0.00016-1>, URL <https://linkinghub.elsevier.com/retrieve/pii/B9780128030110000161>.
- Verrelst, J., Rivera, J.P., Leonenko, G., Alonso, L., Moreno, J., 2014. Optimizing LUT-Based RTM inversion for semiautomatic mapping of crop biophysical parameters from Sentinel-2 and -3 data: Role of cost functions. *IEEE Trans. Geosci. Remote Sens.* 52 (1), 257–269. <http://dx.doi.org/10.1109/TGRS.2013.2238242>, URL <http://ieeexplore.ieee.org/document/6464574>.
- Walter, A., Liebisch, F., Hund, A., 2015. Plant phenotyping: from bean weighing to image analysis. *Plant Methods* 11 (1), 14. <http://dx.doi.org/10.1186/s13007-015-0056-8>.
- Wang, Q., Li, P., 2013. Canopy vertical heterogeneity plays a critical role in reflectance simulation. *Agric. Meteorol.* 169, 111–121. <http://dx.doi.org/10.1016/j.agrformet.2012.10.004>, URL <https://www.sciencedirect.com/science/article/pii/S0168192312002961>.
- Weiss, M., Jacob, F., Duveiller, G., 2020. Remote sensing for agricultural applications: A meta-review. *Remote Sens. Environ.* 236, 111402. <http://dx.doi.org/10.1016/j.rse.2019.111402>, URL <https://www.sciencedirect.com/science/article/pii/S0034425719304213>.
- Wildhaber, S., Graf, L.V., Aasen, H., 2023. Assessing the potential of high-resolution satellite constellations for agricultural monitoring. Munich URL [https://dgp.de/src/tagung/jt2023/proceedings/paper/12\\_dgp2023\\_Wildhaber\\_et\\_al.pdf](https://dgp.de/src/tagung/jt2023/proceedings/paper/12_dgp2023_Wildhaber_et_al.pdf).
- Woche, M., Berger, K., Danner, M., Mauser, W., Hank, T., 2018. Physically-based retrieval of canopy equivalent water thickness using hyperspectral data. *Remote Sens.* 10 (12), 1924. <http://dx.doi.org/10.3390/rs10121924>, URL <https://www.mdpi.com/2072-4292/10/12/1924> Number: 12 Publisher: Multidisciplinary Digital Publishing Institute.
- Woche, M., Berger, K., Danner, M., Mauser, W., Hank, T., 2020. RTM-based dynamic absorption integrals for the retrieval of biochemical vegetation traits. *Int. J. Appl. Earth Obs. Geoinf.* 93, 102219. <http://dx.doi.org/10.1016/j.jag.2020.102219>, URL <https://linkinghub.elsevier.com/retrieve/pii/S0303243420305754>.
- Xie, Q., Dash, J., Huete, A., Jiang, A., Yin, G., Ding, Y., Peng, D., Hall, C.C., Brown, L., Shi, Y., Ye, H., Dong, Y., Huang, W., 2019. Retrieval of crop biophysical parameters from Sentinel-2 remote sensing imagery. *Int. J. Appl. Earth Obs. Geoinf.* 80, 187–195. <http://dx.doi.org/10.1016/j.jag.2019.04.019>, URL <https://www.sciencedirect.com/science/article/pii/S0303243419301199>.
- Younes, N., Joyce, K.E., Maier, S.W., 2021. All models of satellite-derived phenology are wrong, but some are useful: A case study from northern Australia. *Int. J. Appl. Earth Obs. Geoinf.* 97, 102285. <http://dx.doi.org/10.1016/j.jag.2020.102285>, URL <https://linkinghub.elsevier.com/retrieve/pii/S0303243420309284>.
- Zeng, L., Wardlow, B.D., Xiang, D., Hu, S., Li, D., 2020. A review of vegetation phenological metrics extraction using time-series, multispectral satellite data. *Remote Sens. Environ.* 237, 111511. <http://dx.doi.org/10.1016/j.rse.2019.111511>, URL <https://www.sciencedirect.com/science/article/pii/S0034425719305309>.
- Zhao, C., Li, H., Li, P., Yang, G., Gu, X., Lan, Y., 2017. Effect of vertical distribution of crop structure and biochemical parameters of winter wheat on canopy reflectance characteristics and spectral indices. *IEEE Trans. Geosci. Remote Sens.* 55 (1), 236–247. <http://dx.doi.org/10.1109/TGRS.2016.2604492>, Conference Name: IEEE Transactions on Geoscience and Remote Sensing.
- Zhu, Z., Piao, S., Myneni, R.B., Huang, M., Zeng, Z., Canadell, J.G., Ciais, P., Sitch, S., Friedlingstein, P., Arneth, A., Cao, C., Cheng, L., Kato, E., Koven, C., Li, Y., Lian, X., Liu, Y., Liu, R., Mao, J., Pan, Y., Peng, S., Peñuelas, J., Poulter, B., Pugh, T.A.M., Stocker, B.D., Viogy, N., Wang, X., Wang, Y., Xiao, Z., Yang, H., Zaehle, S., Zeng, N., 2016. Greening of the Earth and its drivers. *Nature Clim. Change* 6 (8), 791–795. <http://dx.doi.org/10.1038/nclimate3004>, URL <https://www.nature.com/articles/nclimate3004>.